Spectral Variational Multiscale Model for Transient Dynamics of Phononic Crystals and Acoustic Metamaterials

Ruize Hu and Caglar Oskay*

Department of Civil and Environmental Engineering
Vanderbilt University
Nashville, TN 37235

Abstract

In this manuscript, a spectral multiscale model is developed for transient elastic wave propagation in periodic composites. The basis of the multiscale approach is the variational multiscale enrichment method that permits analysis of wave propagation in the scale-inseparable condition, i.e., short wave propagation. A spectral coarse-scale representation is proposed to capture the salient transient wave phenomena, such as wave dispersion and band gaps that occur in the short wavelength regime. A material-phase-based model basis reduction strategy is devised at the fine scale to achieve computational efficiency. An important feature of the proposed method is that it does not rely on the classical assumption of separation of scales, which permits its application to a broad range of architectured composites including phononic crystals and acoustic metamaterials. Transient elastic wave propagation in two-dimensional periodic structures is investigated. The proposed multiscale approach is verified against direct numerical simulations. The accuracy and computational efficiency of the approach are demonstrated for both phononic crystals and acoustic metamaterials.

Keywords: Multiscale method; Wave propagation; Phononic crystals; Acoustic metamaterials; Spectral finite element; Reduced order model

1 Introduction

Phononic crystals and acoustic metamaterials are architectured composites that exhibit unique capabilities in controlling mechanical waves. Of particular interest is the control of

*Corresponding author address: VU Station B#351831, 2301 Vanderbilt Place, Nashville, TN 37235. Email: caglar.oskay@vanderbilt.edu

band gaps that are generated by Bragg scattering in phononic crystals and local resonance in acoustic metamaterials. Tailoring material microstructures to achieve band gaps in desired frequency ranges presents tremendous potential in novel applications such as elastic cloaking [64], seismic wave mitigation [5, 9], acoustic superlens [40, 35], topological insulators [50, 68] and waveguides [36] among others.

In design and analysis of phononic crystals and acoustic metamaterials, numerical simulations are employed either to characterize the unit cell band structure, or in structural scale wave propagation analyses. The former approach typically characterizes the band gaps of a periodic unit cell based on the Floquet-Bloch theorem. Significant advances have been recently made in efficient computation of dispersion band structures (see Refs. [31, 37]). The structural scale simulation of wave propagation typically relies on the transient dynamic analysis of the structural domain, where the microstructural features are fully resolved [36, 64, 50]. Clearly, the computational cost for such direct numerical simulations is prohibitive particularly when the structural domain size is large compared to that of the microstructure or when the microstructure is complex. This motivates the development of multiscale methods towards modeling the dynamic response of architectured composites in a more computationally efficient manner.

Based on the assumption of scale separation, i.e., the size of microstructures is much smaller than the wavelength, various homogenization approaches have been proposed to model wave propagation in heterogeneous materials. Computational homogenization [57, 62, 41, 42, 60, 61] evaluates nested initial-boundary value problems at the macro- and microscales, which are coupled through the Hill-Mandel energy consistency condition. In the macroscale problem, the constitutive behavior at a quadrature point is obtained through the numerical evaluation of an attached microstructure problem. This approach has been demonstrated to successfully capture the band gaps due to local resonance within acoustic metamaterials, which occur when the macroscopic deformation wavelength is considerably large compared to the size of the microstructure. In contrast, band gaps in phononic crystals occur when the macroscopic wavelength is of the same order as the microstructure size. In order to extend the applicability of homogenization to the short wavelength regime, asymptotic homogenization models with higher-order asymptotic expansions have been proposed [4, 15, 29, 30, 23, 24, 25]. Hu and Oskay [23, 24, 25] recently proposed a nonlocal asymptotic homogenization approach to accurately predict wave propagation in phononic crystals up to the second pass band. Despite significant progress in homogenization-based methods in capturing high frequency dynamics, the applicability of this approach is inherently constrained by the assumption of scale separation. When the deformation wavelength is approaching or smaller than the size of microstructure, the assumption of scale separation is no longer valid. Multiscale methods, such as the elastodynamic homogenization models based on Willis' theory [67, 49, 53, 52, 63, 48],

multiscale finite element method [22, 6, 7] and the method of computational continua [16, 12, 13], that do not rely on the scale separation assumption, offer an alternative pathway to modeling wave propagation in this regime.

Another widely used multiscale method that does not make assumptions on the length scales of continuum models is the variational multiscale method [28]. This framework is based on an additive split of the solution into coarse (resolved) scale and fine (unresolved) scale. The decomposition of solution results in two separate variational equations for the coarse and fine scale, respectively. A crucial step in achieving both accuracy and numerical efficiency using this method is the appropriate evaluation of the fine-scale Green's function. While it can be evaluated analytically for certain problems [54], the analytical form of the Green's function is generally not available when complex physics are involved for 2D and 3D problems. Several variants of the variational multiscale method have been developed employing numerical evaluation of the fine-scale problem to capture the highly complex behavior of heterogeneous materials, including the numerical subgrid upscaling method [1], the stochastic variational multiscale method [2, 17], and the variational multiscale enrichment method [55, 70, 71, 72].

This manuscript proposes a spectral variational multiscale model for transient wave propagation in phononic crystals and acoustic metamaterials. The proposed model is developed based on the variational multiscale enrichment principles [55]. Using the additive split of the displacement field, a system of multiscale governing equations is consistently derived in the variational form. In order to accurately represent wave propagation in short wavelength regimes, we employ spectral representation of the displacement field at the coarse scale. Serendipity elements of up to the septic order are used as the coarse-scale basis. In order to achieve the computational efficiency, a reduced order model is proposed for the fine-scale problem. The model order reduction is achieved using a material-phase-based mode synthesis approach that relies on the Craig-Bampton component mode synthesis [10] and characteristic constraint mode reduction [8]. The proposed model reduction approach efficiently captures the fine-scale transient dynamics with a set of reduced modal basis. To the best of the authors' knowledge, the present work is the first to model transient wave propagation in composite materials using the variational multiscale ideas. A significant advantage of the proposed spectral variational multiscale model compared to the homogenization models is that it is not restricted by the material property contrast of the constituents or scale separation assumption. We demonstrate that the proposed model is effective in transient wave propagation in both phononic crystals and acoustic metamaterials for a broad frequency range.

The remainder of this manuscript is organized as follows: Section 2 derives the two-scale momentum balance equations in variational form. Section 3 presents the discrete multiscale system of equations. Section 4 elaborates the reduced order model for the fine-scale problems. Section 5 provides details in numerical implementation of the proposed model. Section 6

verifies the proposed model in three examples, i.e., unidirectional wave propagation in phononic crystals and acoustic metamaterials, and wave propagation in a 2D phononic crystal waveguide. The accuracy and computational efficiency are examined against direct numerical simulations. The conclusions and future research directions are presented in Section 7.

2 Variational multiscale model for wave propagation

We consider the transient response within a heterogeneous body, $\Omega \in \mathbb{R}^2$, an open and bounded domain constructed by periodic unit cells composed of two or more constituents. Dirichlet and Neumann boundary conditions are respectively applied at $\Gamma^u \subset \partial\Omega$ and $\Gamma^t \subset \partial\Omega$, $\Gamma^t \cap \Gamma^u = \varnothing$ and $\Gamma^t \cup \Gamma^u = \partial\Omega$. The momentum balance equation that governs wave propagation within this body is expressed as:

$$\boldsymbol{\nabla}.\boldsymbol{\sigma}(\mathbf{x},t) = \rho(\mathbf{x})\ddot{\mathbf{u}}(\mathbf{x},t); \quad \mathbf{x} \in \Omega, \quad t \in [0,\ T] \tag{1}$$

where, $\boldsymbol{\sigma}$ denotes the stress tensor; ρ the density; and $\mathbf{u}$ the displacement vector. $\mathbf{x}$ and t are the Cartesian spatial coordinate and time coordinate, respectively. $\boldsymbol{\nabla}.$ is the divergence operator and superimposed dot denotes derivative with respect to time. The constitutive response of the heterogeneous body is described by the generalized Hooke's law:

$$\boldsymbol{\sigma} = \boldsymbol{C}(\mathbf{x}) : \boldsymbol{\epsilon}(\mathbf{x},t) \tag{2}$$

$\boldsymbol{C}$ is the elastic moduli tensor that varies as a function of the position vector to account for the material heterogeneity. $\boldsymbol{\epsilon}$ is the strain tensor under the assumption of small deformation:

$$\boldsymbol{\epsilon} = \boldsymbol{\nabla}^s\mathbf{u} = \frac{1}{2}\left[\boldsymbol{\nabla}\mathbf{u} + (\boldsymbol{\nabla}\mathbf{u})^T\right] \tag{3}$$

where $\boldsymbol{\nabla}$ and $\boldsymbol{\nabla}^s$ are the gradient and symmetric gradient operators, respectively. The boundary and initial conditions are:

$$\text{B.C.} \qquad \mathbf{u}(\mathbf{x},t) = \tilde{\mathbf{u}}(\mathbf{x},t); \quad \mathbf{x} \in \Gamma^u, \qquad \boldsymbol{\sigma}(\mathbf{x},t).\mathbf{n} = \tilde{\mathbf{t}}(\mathbf{x},t); \quad \mathbf{x} \in \Gamma^t \tag{4a}$$

$$\text{I.C.} \qquad \mathbf{u}(\mathbf{x},0) = \mathbf{u}_0; \quad \mathbf{x} \in \Omega, \qquad \dot{\mathbf{u}}(\mathbf{x},0) = \mathbf{v}_0; \quad \mathbf{x} \in \Omega \tag{4b}$$

where $\tilde{\mathbf{u}}$ and $\tilde{\mathbf{t}}$ are respectively the prescribed displacement and traction along the boundary, and $\mathbf{u}_0$ and $\mathbf{v}_0$ are respectively the initial displacement and velocity.

Using the standard arguments, the problem is stated in the variational form:

$$\int_\Omega \mathbf{w}(\mathbf{x}).\left(\rho\ddot{\mathbf{u}}\right)\ d\Omega + \int_\Omega \boldsymbol{\nabla}^s\mathbf{w}(\mathbf{x}) : \boldsymbol{C} : \boldsymbol{\nabla}^s\mathbf{u}\ d\Omega = \int_{\Gamma^t} \mathbf{w}(\mathbf{x}).\tilde{\mathbf{t}}\ d\Gamma \tag{5}$$

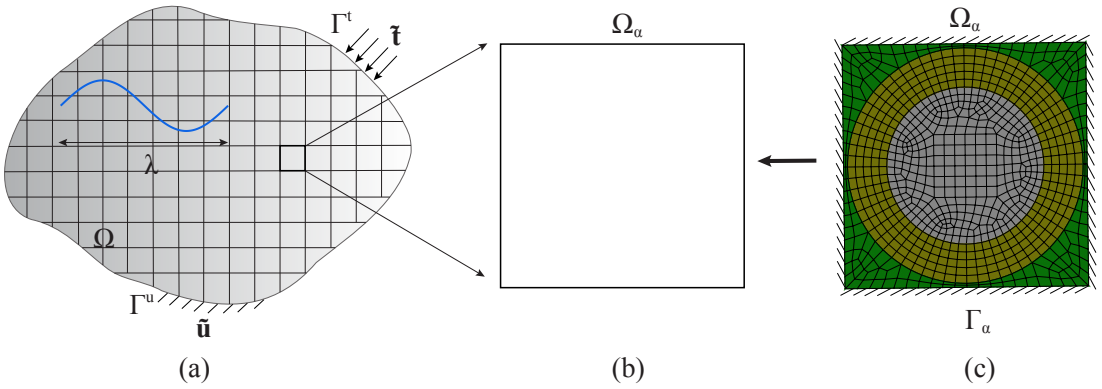

Figure 1: The two-scale problem setting for wave propagation in periodic composites. (a) Composite domain discretized using coarse mesh. (b) One coarse-scale element. (c) The associated fine-scale mesh.

in which, the function spaces for the displacement trial solution and the weighting function are respectively:

$$\mathcal{V} = \left\{ \mathbf{u} \,\middle|\, \mathbf{u} \in \mathcal{H}^1(\Omega),\ \mathbf{u} = \bar{\mathbf{u}} \text{ on } \Gamma^u \right\} \tag{6a}$$

$$\mathcal{W} = \left\{ \mathbf{w} \,\middle|\, \mathbf{w} \in \mathcal{H}^1(\Omega),\ \mathbf{w} = \mathbf{0} \text{ on } \Gamma^u \right\} \tag{6b}$$

where, $\mathcal{H}^1(\Omega)$ is the Sobolev space that contains functions with sufficient smoothness.

We proceed with partitioning the problem domain Ω into n_{nc} non-overlapping open and simply connected subdomains. Each subdomain is one coarse-scale element and align with one unit cell. The interior of the coarse-scale element is denoted as Ω_α and $\bar{\Omega} = \bigcup_{\alpha=1}^{n_{\text{ec}}} \bar{\Omega}_\alpha$, where the overbar indicates the closure of a domain. The choice of using one coarse-scale element to represent one unit cell is made in view of the periodic arrangement of microstructures. Each coarse-scale element can be different when each unit cell contains different microstructures.

The displacement field over the domain Ω is expressed in terms of coarse-scale and fine-scale components through an additive two-scale decomposition:

$$\mathbf{u}(\mathbf{x}, t) = \mathbf{u}^c(\mathbf{x}, t) + \sum_{\alpha=1}^{n_{\text{ec}}} \mathbf{u}_\alpha^f(\mathbf{x}, t) \tag{7}$$

Superscripts c and f denote the coarse and fine scales, respectively. In the classical variational multiscale method, the coarse-scale component approximates the solution resolved by a coarse mesh, whereas the fine-scale component is the associated error. The fine-scale component remains unresolved, and is typically approximated by an analytical function (e.g., residual free bubble function [28]). In the variational multiscale enrichment approach, the fine-scale problem is numerically evaluated, similar to the numerical subgrid upscaling method [1]. For

wave propagation in composites, the material heterogeneity is not resolved at the coarse scale, and $\mathbf{u}^c$ refers to the "homogenized" wave field solution. Numerical solution of $\mathbf{u}_\alpha^f$ captures the rapid wave field oscillations within a coarse-scale element Ω_α, where material heterogeneity is resolved by the fine-scale mesh.

The weighting function is approximated in a similar fashion using a two-scale decomposition:

$$\mathbf{w}(\mathbf{x}) = \mathbf{w}^c(\mathbf{x}) + \sum_{\alpha=1}^{n_{\text{ec}}} \mathbf{w}_\alpha^f(\mathbf{x}) \tag{8}$$

The displacements and weighting functions at the two scales are respectively sought in the function spaces $\mathcal{V}^c$, $\mathcal{W}^c$ and $\mathcal{V}_\alpha^f$, $\mathcal{W}_\alpha^f$. The solution space of the displacement field, $\mathbf{u}$, and weighting function, $\mathbf{w}$, are therefore respectively restricted to the direct sum of the coarse- and fine-scale solution spaces [28]. The fine-scale spaces are defined such that the trial solution and the weighting function are localized within the corresponding coarse-scale element Ω_α and vanish elsewhere:

$$\mathcal{V}_\alpha^f = \mathcal{W}_\alpha^f = \left\{ {\mathbf{v}_\alpha}^f \,\middle|\, \mathbf{v}_\alpha^f = \mathbf{0} \text{ on } \bar{\Omega} \setminus \Omega_\alpha \right\} \tag{9}$$

The function spaces for the finite dimensional approximation to the coarse-scale fields are chosen as C^0 continuous:

$$\mathcal{V}^c = \left\{ \mathbf{u}^c \,\middle|\, \mathbf{u}^c \in C^0(\Omega) \cap \mathcal{V},\ \mathbf{u}^c(\Omega_\alpha) \in \mathcal{P}^p(\Omega_\alpha) \right\} \tag{10a}$$

$$\mathcal{W}^c = \left\{ \mathbf{w}^c \,\middle|\, \mathbf{w}^c \in C^0(\Omega) \cap \mathcal{W},\ \mathbf{w}^c(\Omega_\alpha) \in \mathcal{P}^p(\Omega_\alpha) \right\} \tag{10b}$$

where $\mathcal{P}^p(\Omega_\alpha)$ denotes the set of complete polynomials of order p over Ω_α. This choice for the coarse-scale displacement field indicates that high-order spectral functions are admissible within each element, whereas the displacement is C^0 continuous across the element interfaces.

Remark 1. The approximation space defined in Eq. 9 implies the fine-scale homogeneous Dirichlet boundary conditions along the boundaries of Ω_α. This boundary condition is widely used [46, 47, 55, 71] due to its simplicity and is adopted in this study. We note that other fine-scale boundary conditions can also be applied, such as, mixed boundary conditions [56, 70], edge bubbles for interface problems [66], and mixed use of bubbles and other Dirichlet boundary conditions for strain localization problems [19]. While these boundary conditions may improve the numerical accuracy, the possible interactions of the fine-scale problems between neighboring coarse-scale elements may result in significant complexity in numerical implementation and increased computational cost.

Substituting the two-scale decompositions (Eqs. 7, 8) into Eq. 5, the variational form is

decomposed into a coarse-scale problem defined over Ω and a series of fine-scale problems defined within each coarse-scale element Ω_α. At the coarse scale:

$$\int_\Omega \mathbf{w}^c.\left(\rho\ddot{\mathbf{u}}^c\right)\ d\Omega + \int_\Omega \boldsymbol{\nabla}^s\mathbf{w}^c : \boldsymbol{C} : \boldsymbol{\nabla}^s\mathbf{u}^c\ d\Omega\ = \\ -\sum_{\alpha=1}^{n_{\text{ec}}}\int_{\Omega_\alpha}\mathbf{w}^c.\left(\rho\ddot{\mathbf{u}}_\alpha^f\right)\ d\Omega_\alpha - \sum_{\alpha=1}^{n_{\text{ec}}}\int_{\Omega_\alpha}\boldsymbol{\nabla}^s\mathbf{w}^c : \boldsymbol{C} : \boldsymbol{\nabla}^s\mathbf{u}_\alpha^f\ d\Omega_\alpha\ + \int_{\Gamma^t}\mathbf{w}^c.\tilde{\mathbf{t}}\ d\Gamma \quad (11)$$

The terms on the left hand side are the virtual kinetic energy and strain energy, whereas the first two terms on the right hand side describe the total coarse-scale virtual work due to fine-scale dynamics within all coarse-scale elements. At the fine scale, the variational form for Ω_α, is:

$$\int_{\Omega_\alpha}\mathbf{w}^f.\left(\rho\ddot{\mathbf{u}}^f\right)\ d\Omega_\alpha + \int_{\Omega_\alpha}\boldsymbol{\nabla}^s\mathbf{w}^f : \boldsymbol{C} : \boldsymbol{\nabla}^s\mathbf{u}^f\ d\Omega_\alpha\ = \\ -\int_{\Omega_\alpha}\mathbf{w}^f.\left(\rho\ddot{\mathbf{u}}^c\right)\ d\Omega_\alpha - \int_{\Omega_\alpha}\boldsymbol{\nabla}^s\mathbf{w}^f : \boldsymbol{C} : \boldsymbol{\nabla}^s\mathbf{u}^c\ d\Omega_\alpha \quad (12)$$

The traction term is not present in Eq. 12 because the fine-scale weighting function vanishes at all coarse-scale element domain boundaries via Eq. 9. The fine-scale problem states that the virtual kinetic energy and strain energy of each coarse-scale element domain at the fine scale is balanced with the local virtual work due to the dynamics of the coarse-scale. Equations 11 and 12 constitute a coupled problem for evaluating the dynamic response of the composite domain.

In what follows, we provide an approach to directly evaluate this system of equations. It is important to highlight that the direct evaluation of this system does not reduce the computational cost compared with the direct numerical simulation of the governing equation, Eq. 5. Alternatively, direct evaluation of the two-scale system forms the foundation for the reduced basis approximation we later introduce for the fine-scale problem.

3 Spectral variational multiscale model

In this section, we propose a spectral approach to capture the transient dynamic response of periodic composites by numerically evaluating the coarse- and fine-scale variational forms provided in Eqs. 11 and 12.

The selection of the size of coarse-scale element and the order of the corresponding shape functions depends on the characteristic wavelength of the associated problem. For static problems [70, 71], the wavelength is infinitely long and it typically suffices to use linear elements at the coarse scale. For wave propagation problems, sufficiently fine resolution is necessary

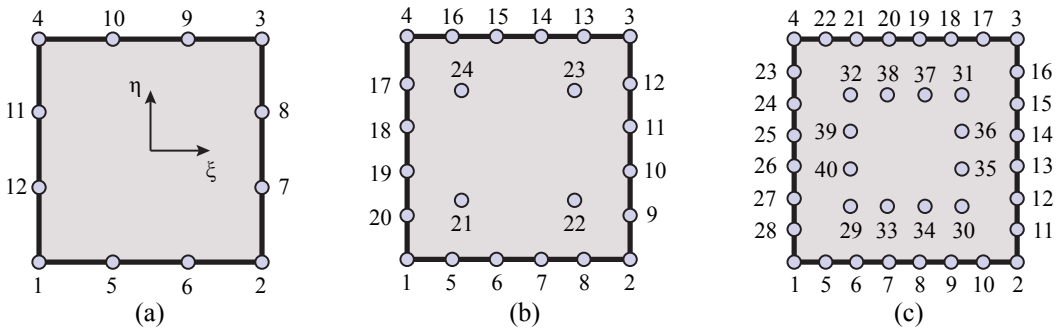

Figure 2: Quadrilateral serendipity elements of (a) cubic (3^{rd}), (b) quintic (5^{th}) and (c) septic (7^{th}) orders.

to accurately capture the wave field and avoid numerical dispersion [11]. Fine resolution can be achieved through h-refinement or p-refinement, and their application in dynamic problems has been extensively discussed in the literature in the context of single scale analysis (see e.g., Refs. [65, 3, 32, 33, 34]). In the proposed multiscale model, the size of the coarse-scale elements is fixed to the size of the underlying microstructure. We employ high order shape functions to accurately capture high frequency wave propagation through a p-refinement strategy at the coarse scale.

Lagrange polynomials are used as shape functions for the coarse-scale elements. In two dimensions, the classical quadrilateral Lagrange elements contain $(p+1)^2$ nodes. Due to the presence of large numbers of bubble nodes, Lagrange elements pose significant computational cost for higher spectral orders. Instead, serendipity quadrilateral elements achieve the same order of approximation with fewer nodes. The higher-order serendipity elements developed in Refs. [58, 59] are adopted herein. In this family of serendipity elements, the number of nodes is minimized while maintaining the required polynomial completeness. Figure 2 shows the elements of cubic, quintic and septic orders, which respectively have 12, 24 and 40 nodes per element. The formulas for the shape functions and locations of the nodal points are provided in Ref. [58].

The fine-scale trial solution and weighting function are approximated using standard bilinear finite elements. This selection of fine-scale elements has also been used in Refs. [18, 56]. Along with the homogeneous Dirichlet type fine-scale boundary conditions, this choice ensures linear independence of the solution spaces at the coarse and fine scales and the direct sum relationship between the multiscale fields is valid.

Employing the classical Bubnov-Galerkin approach, the coarse-scale displacement, weight-

ing function and their gradients within a coarse-scale element are written as:

$$\mathbf{u}^c_\alpha = \mathbf{N}^c_\alpha \mathbf{d}^c_\alpha = \mathbf{N}^c_\alpha \mathbf{L}^c_\alpha \mathbf{d}^c; \quad \mathbf{w}^c_\alpha = \mathbf{N}^c_\alpha \mathbf{c}^c_\alpha = \mathbf{N}^c_\alpha \mathbf{L}^c_\alpha \mathbf{c}^c \tag{13a}$$

$$[\boldsymbol{\nabla}^s \mathbf{u}^c_\alpha] = \mathbf{B}^c_\alpha \mathbf{d}^c_\alpha = \mathbf{B}^c_\alpha \mathbf{L}^c_\alpha \mathbf{d}^c; \quad [\boldsymbol{\nabla}^s \mathbf{w}^c_\alpha] = \mathbf{B}^c_\alpha \mathbf{c}^c_\alpha = \mathbf{B}^c_\alpha \mathbf{L}^c_\alpha \mathbf{c}^c \tag{13b}$$

where, $\mathbf{u}^c_\alpha(\mathbf{x}, t) := \mathbf{u}^c(\mathbf{x} \in \Omega_\alpha, t)$ with the corresponding weighting function analogously defined. $\mathbf{N}^c_\alpha$ and $\mathbf{B}^c_\alpha$ are respectively the coarse-scale element shape function matrix and strain-displacement matrix (detailed definition of these matrices is provided in Ref. [14]) within the coarse-scale element, Ω_α. Einstein summation does not apply to the subscripts. The square bracket indicates the vectorized form of the corresponding tensors. $\mathbf{d}^c_\alpha$ and $\mathbf{c}^c_\alpha$ are the element nodal displacement and weighting function vectors, and they are related to the global vectors, $\mathbf{d}^c$ and $\mathbf{c}^c$, through the mapping matrix $\mathbf{L}^c_\alpha$, which assembles the global vectors from the element vectors [14].

Each coarse-scale element is associated with a heterogeneous microstructure (also denoted as Ω_α in Fig. 1). Equation 12 is evaluated to compute the fine-scale fields for all microstructures within the problem domain. Consider the discretization of the microstructure, Ω_α into n_{ef} fine-scale elements. The fine-scale displacement, weighting function and their gradients for the fine-scale element e within the microstructure Ω_α are expressed as:

$$\mathbf{u}^f_{e,\alpha} = \mathbf{N}^f_{e,\alpha} \mathbf{d}^f_{e,\alpha} = \mathbf{N}^f_{e,\alpha} \mathbf{L}^f_{e,\alpha} \mathbf{d}^f_\alpha; \quad \mathbf{w}^f_{e,\alpha} = \mathbf{N}^f_{e,\alpha} \mathbf{c}^f_{e,\alpha} = \mathbf{N}^f_{e,\alpha} \mathbf{L}^f_{e,\alpha} \mathbf{c}^f_\alpha \tag{14a}$$

$$\left[\boldsymbol{\nabla}^s \mathbf{u}^f_{e,\alpha}\right] = \mathbf{B}^f_{e,\alpha} \mathbf{d}^f_{e,\alpha} = \mathbf{B}^f_{e,\alpha} \mathbf{L}^f_{e,\alpha} \mathbf{d}^f_\alpha; \quad \left[\boldsymbol{\nabla}^s \mathbf{w}^f_{e,\alpha}\right] = \mathbf{B}^f_{e,\alpha} \mathbf{c}^f_{e,\alpha} = \mathbf{B}^f_{e,\alpha} \mathbf{L}^f_{e,\alpha} \mathbf{c}^f_\alpha \tag{14b}$$

where, $\mathbf{N}^f_{e,\alpha}$ and $\mathbf{B}^f_{e,\alpha}$ are respectively the fine-scale element shape function matrix and strain-displacement matrix within the fine-scale element, Ω^e_α. $\mathbf{d}^f_{e,\alpha}$ and $\mathbf{c}^f_{e,\alpha}$ are the fine-scale element nodal displacement and weighting vectors, related to the vector of the fine-scale nodal displacement and weighting functions within the microstructure through $\mathbf{L}^f_{e,\alpha}$. Employing Eqs. 13 and 14, the discretized forms of Eqs. 11 and 12 are obtained as:

$$\mathbf{K}^{cc}\mathbf{d}^c + \mathbf{M}^{cc}\ddot{\mathbf{d}}^c + \sum_{\alpha=1}^{n_{\text{ec}}} \mathbf{K}^{cf_\alpha}\mathbf{d}^{f_\alpha} + \sum_{\alpha=1}^{n_{\text{ec}}} \mathbf{M}^{cf_\alpha}\ddot{\mathbf{d}}^{f_\alpha} = \mathbf{F}^c \tag{15a}$$

$$\mathbf{K}^{f_\alpha c}\mathbf{d}^c + \mathbf{M}^{f_\alpha c}\ddot{\mathbf{d}}^c + \mathbf{K}^{f_\alpha f_\alpha}\mathbf{d}^{f_\alpha} + \mathbf{M}^{f_\alpha f_\alpha}\ddot{\mathbf{d}}^{f_\alpha} = \mathbf{0}, \quad \alpha = 1, ..., n_{\text{ec}} \tag{15b}$$

where, $\mathbf{K}^{f_\alpha f_\alpha}$, $\mathbf{M}^{f_\alpha f_\alpha}$ and $\mathbf{K}^{cc}$, $\mathbf{M}^{cc}$ are respectively the stiffness and mass matrices of the fine-scale problem in Ω_α and the coarse-scale problem. $\mathbf{K}^{cf_\alpha}$ and $\mathbf{M}^{cf_\alpha}$ are the stiffness and mass matrices due to interactions between the two scales. $\mathbf{F}^c$ is the coarse-scale force vector.

They are obtained by assembling the element matrices and the force vectors as:

$$\mathbf{K}^{f_\alpha f_\alpha} = \sum_{e=1}^{n_{\text{ef}}} \left(\mathbf{L}^f_{e,\alpha}\right)^T \mathbf{K}^{f_\alpha f_\alpha}_e \mathbf{L}^f_{e,\alpha}; \quad \mathbf{M}^{f_\alpha f_\alpha} = \sum_{e=1}^{n_{\text{ef}}} \left(\mathbf{L}^f_{e,\alpha}\right)^T \mathbf{M}^{f_\alpha f_\alpha}_e \mathbf{L}^f_{e,\alpha} \tag{16a}$$

$$\mathbf{K}^{cc} = \sum_{\alpha=1}^{n_{\text{ec}}} (\mathbf{L}^c_\alpha)^T \mathbf{K}^{cc}_\alpha \mathbf{L}^c_\alpha; \quad \mathbf{M}^{cc} = \sum_{\alpha=1}^{n_{\text{ec}}} (\mathbf{L}^c_\alpha)^T \mathbf{M}^{cc}_\alpha \mathbf{L}^c_\alpha \tag{16b}$$

$$\mathbf{K}^{cf_\alpha} = \left(\mathbf{K}^{f_\alpha c}\right)^T = (\mathbf{L}^c_\alpha)^T \sum_{e=1}^{n_{\text{ef}}} \mathbf{K}^{cf_\alpha}_e \mathbf{L}^f_{e,\alpha}; \quad \mathbf{M}^{cf_\alpha} = \left(\mathbf{M}^{f_\alpha c}\right)^T = (\mathbf{L}^c_\alpha)^T \sum_{e=1}^{n_{\text{ef}}} \mathbf{M}^{cf_\alpha}_e \mathbf{L}^f_{e,\alpha} \tag{16c}$$

$$\mathbf{F}^c = \sum_{\alpha=1}^{n_{\text{ec}}} (\mathbf{L}^c_\alpha)^T \mathbf{f}_\alpha \tag{16d}$$

n_{ef} is the number of fine-scale elements used to discretize Ω_α. The element matrices and the force vector are:

$$\mathbf{K}^{cc}_\alpha = \int_{\Omega_\alpha} (\mathbf{B}^c_\alpha)^T \mathbf{C}(\mathbf{x}) \mathbf{B}^c_\alpha \, d\Omega_\alpha; \quad \mathbf{M}^{cc}_\alpha = \int_{\Omega_\alpha} (\mathbf{N}^c_\alpha)^T \rho(\mathbf{x}) \mathbf{N}^c_\alpha \, d\Omega_\alpha \tag{17a}$$

$$\mathbf{K}^{f_\alpha f_\alpha}_e = \int_{\Omega^e_\alpha} (\mathbf{B}^f_{e,\alpha})^T \mathbf{C}_e \mathbf{B}^f_{e,\alpha} \, d\Omega^e_\alpha; \quad \mathbf{M}^{f_\alpha f_\alpha}_e = \int_{\Omega^e_\alpha} (\mathbf{N}^f_{e,\alpha})^T \rho_e \mathbf{N}^f_{e,\alpha} \, d\Omega^e_\alpha \tag{17b}$$

$$\mathbf{K}^{cf_\alpha}_e = \int_{\Omega^e_\alpha} (\mathbf{B}^c_{e,\alpha})^T \mathbf{C}_e \mathbf{B}^f_{e,\alpha} \, d\Omega^e_\alpha; \quad \mathbf{M}^{cf_\alpha}_e = \int_{\Omega^e_\alpha} (\mathbf{N}^c_{e,\alpha})^T \rho_e \mathbf{N}^f_{e,\alpha} \, d\Omega^e_\alpha \tag{17c}$$

$$\mathbf{f}_\alpha = \int_{\Gamma^t_\alpha} (\mathbf{N}^c_\alpha)^T \, \tilde{\mathbf{t}} \, d\Gamma^t_\alpha \tag{17d}$$

where $\mathbf{C}_e$ and ρ_e are respectively the elastic moduli and density of the e^{th} fine-scale element. The evaluation of the pure fine-scale matrices in Eq. 17b and the coarse-scale force vector in Eq. 17d is straightforward and performed using the standard element level integration procedure. Evaluating Eqs. 17a and c is not standard and the detailed evaluation procedure for coarse-scale and scale interaction matrices is provided in Section 5.2.

The construction of global matrices constitutes the assembly of the coarse-scale stiffness and mass matrices and the corresponding fine-scale matrices of all subdomains. The global displacement vector that contains coarse-scale and fine-scale degrees of freedom (DOFs) are arranged as follows:

$$\mathbf{d}_{SVM} = \left[(\mathbf{d}^c)^T, \, \left(\mathbf{d}^{f_1}\right)^T, \, \left(\mathbf{d}^{f_2}\right)^T, \, ..., \, \left(\mathbf{d}^{f_{n_{\text{ec}}}}\right)^T \right]^T \tag{18}$$

Accordingly, the global stiffness matrix is constructed by block assembly of the coarse-scale,

fine-scale and the interaction matrices (Eqs. 17a-c) of all microstructures:

$$\mathbf{K}_{SVM} = \begin{bmatrix} \mathbf{K}^{cc} & \mathbf{K}^{cf_1} & \mathbf{K}^{cf_2} & \dots & \mathbf{K}^{cf_{n_{\text{ec}}}} \\ \mathbf{K}^{f_1c} & \mathbf{K}^{f_1f_1} & \mathbf{0} & \dots & \mathbf{0} \\ \mathbf{K}^{f_2c} & \mathbf{0} & \mathbf{K}^{f_2f_2} & \dots & \mathbf{0} \\ \vdots & \vdots & \vdots & \ddots & \vdots \\ \mathbf{K}^{f_{n_{\text{ec}}}c} & \mathbf{0} & \mathbf{0} & \dots & \mathbf{K}^{f_{n_{\text{ec}}}f_{n_{\text{ec}}}} \end{bmatrix} \tag{19}$$

The global mass matrix is assembled similarly. The global force vector has the form: $\mathbf{F}_{SVM} = \left[(\mathbf{F}^c)^T,\ \mathbf{0}^T,\ \mathbf{0}^T,\ ...,\ \mathbf{0}^T\right]^T$. The DOFs associated with Dirichlet boundary conditions of both coarse and fine scales are eliminated using static condensation. The resulting global system of equations is:

$$\mathbf{K}_{SVM}\mathbf{d}_{SVM} + \mathbf{M}_{SVM}\ddot{\mathbf{d}}_{SVM} = \mathbf{F}_{SVM} \tag{20}$$

Equation 20 constitutes the full system of equations of the spectral variational multiscale (SVM) model for wave propagation in periodic composites, where the dynamics at both scales are fully resolved.

4 Phase mode synthesis for basis reduction at fine scale

Evaluating Eq. 20 directly does not provide significant numerical efficiency compared to single scale finite element simulation when the same level of mesh density is used to discretize the microstructure. The multiscale system of equations have slightly fewer DOFs since the boundary DOFs at the fine scale are condensed out. Nevertheless, the system size remains relatively large. In this section, we propose a basis reduction strategy at the fine scale to improve the computational efficiency.

The basis reduction at the fine scale is performed as a two-step component mode synthesis procedure that combines the Craig-Bampton method [10] and the characteristic constraint mode reduction [8], which were originally developed for reduced representation of structural components in analyzing the vibration response of large-scale structural systems. The key idea in this approach is that the dynamic behavior of a structural system is decomposed into its structural components. In classical analysis of structural system using Craig-Bampton method, the dynamic response of each system component is expressed as the superposition of its internal dynamics with the component-structure interface fixed, and the static response of the component due to the deformation of the component-structure interface. The internal dynamics of the component is approximated using a truncated modal basis. The constraint

mode reduction refers to a reduced modal basis representation of the deformation along the component-structure interface.

We adopt this idea in the analysis of the fine-scale problem and employ a phase-based basis reduction approach. In this context, the subdomains of the microstructure that are occupied by separate constituent materials (i.e., phases) are considered as the "components". The material interfaces become the "component-structure interfaces". Craig-Bampton mode synthesis is employed to express the response of each material phase using a truncated set of modal basis functions. The interface degrees of freedom are then reduced through constraint mode reduction.

Consider a microstructure Ω_α that consists of n^{ph} material phases and n^{int} interfaces. The interfaces are assumed to be non-intersecting, and separate only two phases. The fine-scale stiffness matrix of each microstructure $\mathbf{K}^{ff}$ (subscript α is omitted for clarity) is partitioned and rearranged as follows:

$$\mathbf{K}^{ff} = \begin{bmatrix} \mathbf{K}^{P_1P_1} & \mathbf{0} & \dots & \mathbf{0} & \mathbf{K}^{P_1I_1} & \mathbf{K}^{P_1I_2} & \dots & \mathbf{K}^{P_1I_{n^{\text{int}}}} \\ \mathbf{0} & \mathbf{K}^{P_2P_2} & \dots & \mathbf{0} & \mathbf{K}^{P_2I_1} & \mathbf{K}^{P_2I_2} & \dots & \mathbf{K}^{P_2I_{n^{\text{int}}}} \\ \vdots & \vdots & \ddots & \vdots & \vdots & \vdots & \ddots & \vdots \\ \mathbf{0} & \mathbf{0} & \dots & \mathbf{K}^{P_{n^{\text{ph}}}P_{n^{\text{ph}}}} & \mathbf{K}^{P_{n^{\text{ph}}}I_1} & \mathbf{K}^{P_{n^{\text{ph}}}I_2} & \dots & \mathbf{K}^{P_{n^{\text{ph}}}I_{n^{\text{int}}}} \\ \mathbf{K}^{I_1P_1} & \mathbf{K}^{I_1P_2} & \dots & \mathbf{K}^{I_1P_{n^{\text{ph}}}} & \mathbf{K}^{I_1I_1} & \mathbf{0} & \dots & \mathbf{0} \\ \mathbf{K}^{I_2P_1} & \mathbf{K}^{I_2P_2} & \dots & \mathbf{K}^{I_2P_{n^{\text{ph}}}} & \mathbf{0} & \mathbf{K}^{I_2I_2} & \dots & \mathbf{0} \\ \vdots & \vdots & \ddots & \vdots & \vdots & \vdots & \ddots & \vdots \\ \mathbf{K}^{I_{n^{\text{int}}}P_1} & \mathbf{K}^{I_{n^{\text{int}}}P_2} & \dots & \mathbf{K}^{I_{n^{\text{int}}}P_{n^{\text{ph}}}} & \mathbf{0} & \mathbf{0} & \dots & \mathbf{K}^{I_{n^{\text{int}}}I_{n^{\text{int}}}} \end{bmatrix} \tag{21}$$

where $\mathbf{K}^{P_iP_i}$ and $\mathbf{K}^{I_jI_j}$ are the matrix blocks associated with phase P_i and interface I_j, respectively. $\mathbf{K}^{P_iI_j} = \left(\mathbf{K}^{I_jP_i}\right)^T$ denotes the interaction matrix between phase P_i and interface I_j. The mass matrix $\mathbf{M}^{ff}$ is partitioned and rearranged similarly. Equation 21 is a reordered version of the classical finite element stiffness matrix. With homogeneous Dirichlet boundary conditions used, the matrix has full rank and is invertible.

Equation 21 shows the general structure of the fine-scale stiffness matrix of a multi-phase microstructure, where the fine-scale mesh conforms to the material interfaces and the interfaces do not intersect. The type of microstructures under these restrictions cover a broad class of phononic crystal and acoustic metamaterial designs [44, 45]. For these microstructures, sufficiently fine mesh ensures that the DOFs of two different interfaces do not have direct interactions, therefore, $\mathbf{K}^{I_iI_j} = \mathbf{0}$, $i \neq j$. In addition, $\mathbf{K}^{P_iI_j} = \mathbf{0}$ when phase P_i is not connected with interface I_j.

The overall strategy for the material-phase-based mode synthesis is illustrated in Fig. 3. Using the Craig-Bampton (CB) method [10], the dynamic response of the microstructure is

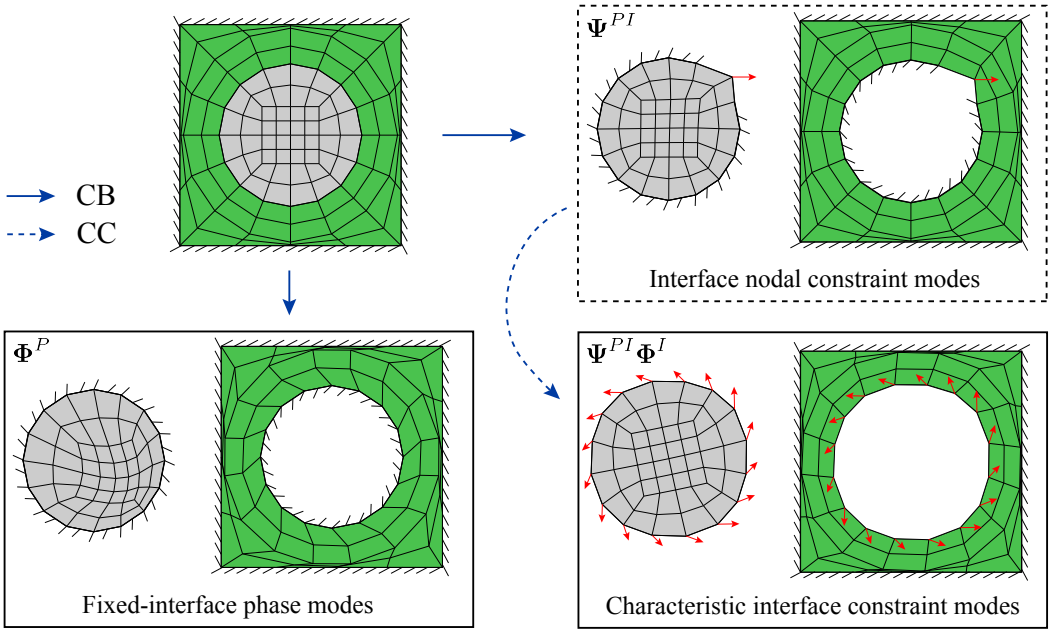

Figure 3: Material-phase-based mode synthesis strategy.

expressed in terms of a truncated set of fixed-interface normal modes of each material phase and the interface nodal constraint modes. The characteristic constraint (CC) mode synthesis is then employed to represent the interface deformation using a truncated set of characteristic interface constraint modes. The normal modes of a material phase P_i, $i = 1, ..., n^{\text{ph}}$, are obtained by solving the eigenvalue problem:

$$\left(\mathbf{K}^{P_iP_i} - \lambda^{P_i}\mathbf{M}^{P_iP_i}\right)\boldsymbol{\phi}^{P_i} = \mathbf{0} \tag{22}$$

All boundaries of the phase are fixed. Solving Eq. 22 results in m^{P_i} normal modes and they are sorted according to their corresponding eigenvalues in the ascending order: $\{\boldsymbol{\phi}_1^{P_i}, \boldsymbol{\phi}_2^{P_i}, ..., \boldsymbol{\phi}_{m^{P_i}}^{P_i}\}$. Model order reduction is achieved by selecting a truncated set of normal modes as basis for the solution of the dynamics within phase P_i. The lowest l^{P_i} modes are selected to form the normal mode matrix: $\boldsymbol{\Phi}^{P_i} = \left[\boldsymbol{\phi}_1^{P_i}, \boldsymbol{\phi}_2^{P_i}, ..., \boldsymbol{\phi}_{l^{P_i}}^{P_i}\right]$.

The effect of deformation along an interface on the adjacent material phases is taken into account by considering the static interface constraint modes. The interface modes are computed by evaluating the static deformation of phase P_i subjected to perturbations along the interface I_j. Let $\boldsymbol{\Psi}^{P_iI_j}$ denote the interface constraint mode matrix. Each column in the constraint mode matrix contains the nodal displacements in phase P_i subjected to a unit displacement applied at an interface node along one spatial direction while all other interface nodal DOFs are set to vanish. It is straightforward to show that the interface constraint mode

matrix is expressed as:

$$\mathbf{\Psi}^{P_i I_j} = -\left(\mathbf{K}^{P_i P_i}\right)^{-1} \mathbf{K}^{P_i I_j} \tag{23}$$

The fine-scale DOFs within each material phase is represented using the generalized basis that is composed of the fixed-interface normal modes and the interface constraint modes. The original DOFs are related to the reduced DOFs by the modal transformation matrix $\mathbf{T}^P$:

$$\mathbf{T}^P = \begin{bmatrix} \mathbf{\Phi}^{P_1} & \mathbf{0} & \dots & \mathbf{0} & \mathbf{\Psi}^{P_1 I_1} & \mathbf{\Psi}^{P_1 I_2} & \dots & \mathbf{\Psi}^{P_1 I_{n^{\text{int}}}} \\ \mathbf{0} & \mathbf{\Phi}^{P_2} & \dots & \mathbf{0} & \mathbf{\Psi}^{P_2 I_1} & \mathbf{\Psi}^{P_2 I_2} & \dots & \mathbf{\Psi}^{P_2 I_{n^{\text{int}}}} \\ \vdots & \vdots & \ddots & \vdots & \vdots & \vdots & \ddots & \vdots \\ \mathbf{0} & \mathbf{0} & \dots & \mathbf{\Phi}^{P_{n^{\text{ph}}}} & \mathbf{\Phi}^{P_{n^{\text{ph}}} I_1} & \mathbf{\Phi}^{P_{n^{\text{ph}}} I_2} & \dots & \mathbf{\Phi}^{P_{n^{\text{ph}}} I_{n^{\text{int}}}} \\ \mathbf{0} & \mathbf{0} & \dots & \mathbf{0} & \mathbf{I}^{I_1} & \mathbf{0} & \dots & \mathbf{0} \\ \mathbf{0} & \mathbf{0} & \dots & \mathbf{0} & \mathbf{0} & \mathbf{I}^{I_2} & \dots & \mathbf{0} \\ \vdots & \vdots & \ddots & \vdots & \vdots & \vdots & \ddots & \vdots \\ \mathbf{0} & \mathbf{0} & \dots & \mathbf{0} & \mathbf{0} & \mathbf{0} & \dots & \mathbf{I}^{I_{n^{\text{int}}}} \end{bmatrix} \tag{24}$$

where $\mathbf{I}^{I_j}$ is the identity matrix of the same size as $\mathbf{K}^{I_j I_j}$. Applying this transformation to the fine-scale stiffness and mass matrix:

$$\mathbf{K}_{R1}^{ff} = \left(\mathbf{T}^P\right)^T \mathbf{K}^{ff} \mathbf{T}^P \tag{25a}$$

$$\mathbf{M}_{R1}^{ff} = \left(\mathbf{T}^P\right)^T \mathbf{M}^{ff} \mathbf{T}^P \tag{25b}$$

$\mathbf{K}_{R1}^{ff}$ and $\mathbf{M}_{R1}^{ff}$ are the reduced stiffness and mass matrices due to the truncated selection of normal modes of each material phase.

While the above procedure reduces the degrees of freedom within each material phase, the number of interface degrees of freedom can be significant, especially for complex microstructures where a fine mesh is required at the interface region. We perform a secondary model order reduction using the characteristic constraint mode reduction approach [8]. The interface degrees of freedom is reduced by using truncated normal modes to represent the interface dynamics. The normal modes of interface I_j are computed by the eigenvalue analysis of the interface partition of $\mathbf{K}_{R1}^{ff}$ and $\mathbf{M}_{R1}^{ff}$:

$$\left(\mathbf{K}_{R1}^{I_j I_j} - \lambda^{I_j} \mathbf{M}_{R1}^{I_j I_j}\right) \boldsymbol{\phi}^{I_j} = \mathbf{0} \tag{26}$$

The reduced basis is obtained by sorting the interface normal modes and selecting those with the lowest l^{I_j} eigenvalues to construct the interface normal mode matrix: $\mathbf{\Phi}^{I_j} = \left[\boldsymbol{\phi}_1^{I_j}, \boldsymbol{\phi}_2^{I_j}, ..., \boldsymbol{\phi}_{l^{I_j}}^{I_j}\right]$.

The interface modal transformation matrix is defined as:

$$\mathbf{T}^I = \begin{bmatrix} \boldsymbol{I}_{R_1}^{P_1} & \mathbf{0} & \dots & \mathbf{0} & \mathbf{0} & \mathbf{0} & \dots & \mathbf{0} \\ \mathbf{0} & \boldsymbol{I}_{R_1}^{P_2} & \dots & \mathbf{0} & \mathbf{0} & \mathbf{0} & \dots & \mathbf{0} \\ \vdots & \vdots & \ddots & \vdots & \vdots & \vdots & \ddots & \vdots \\ \mathbf{0} & \mathbf{0} & \dots & \boldsymbol{I}_{R_1}^{P_{n^{\text{ph}}}} & \mathbf{0} & \mathbf{0} & \dots & \mathbf{0} \\ \mathbf{0} & \mathbf{0} & \dots & \mathbf{0} & \boldsymbol{\Phi}^{I_1} & \mathbf{0} & \dots & \mathbf{0} \\ \mathbf{0} & \mathbf{0} & \dots & \mathbf{0} & \mathbf{0} & \boldsymbol{\Phi}^{I_2} & \dots & \mathbf{0} \\ \vdots & \vdots & \ddots & \vdots & \vdots & \vdots & \ddots & \vdots \\ \mathbf{0} & \mathbf{0} & \dots & \mathbf{0} & \mathbf{0} & \mathbf{0} & \dots & \boldsymbol{\Phi}^{I_{n^{\text{int}}}} \end{bmatrix} \tag{27}$$

where $\boldsymbol{I}_{R_1}^{P_i}$ is the identity matrix of the same size as the partition of the reduced stiffness matrix corresponding to the i^{th} material phase, $\mathbf{K}_{R_1}^{P_i P_i}$. The secondary reduction to the stiffness and mass matrix is obtained by:

$$\mathbf{K}_{R2}^{ff} = \left(\mathbf{T}^I\right)^T \mathbf{K}_{R1}^{ff} \mathbf{T}^I = \left(\mathbf{T}^P \mathbf{T}^I\right)^T \mathbf{K}^{ff} \mathbf{T}^P \mathbf{T}^I \tag{28a}$$

$$\mathbf{M}_{R2}^{ff} = \left(\mathbf{T}^I\right)^T \mathbf{M}_{R1}^{ff} \mathbf{T}^I = \left(\mathbf{T}^P \mathbf{T}^I\right)^T \mathbf{M}^{ff} \mathbf{T}^P \mathbf{T}^I \tag{28b}$$

The coarse-fine interaction matrices in Eq. 15 are reduced similarly by post-multiplying the phase and interface modal transformation matrices:

$$\mathbf{K}_{R2}^{cf_\alpha} = \left(\mathbf{K}_{R2}^{f_\alpha c}\right)^T = \mathbf{K}^{cf_\alpha} \mathbf{T}^P \mathbf{T}^I \tag{29a}$$

$$\mathbf{M}_{R2}^{cf_\alpha} = \left(\mathbf{M}_{R2}^{f_\alpha c}\right)^T = \mathbf{M}^{cf_\alpha} \mathbf{T}^P \mathbf{T}^I \tag{29b}$$

The reduced order multiscale system of equations is written as:

$$\mathbf{K}^{cc}\mathbf{d}^c + \mathbf{M}^{cc}\ddot{\mathbf{d}}^c + \sum_{\alpha=1}^{n_{\text{ec}}} \mathbf{K}_{R2}^{cf_\alpha}\mathbf{g}^{f_\alpha} + \sum_{\alpha=1}^{n_{\text{ec}}} \mathbf{M}_{R2}^{cf_\alpha}\ddot{\mathbf{g}}^{f_\alpha} = \mathbf{F}^c \tag{30a}$$

$$\mathbf{K}_{R2}^{f_\alpha c}\mathbf{d}^c + \mathbf{M}_{R2}^{f_\alpha c}\ddot{\mathbf{d}}^c + \mathbf{K}_{R2}^{f_\alpha f_\alpha}\mathbf{g}^{f_\alpha} + \mathbf{M}_{R2}^{f_\alpha f_\alpha}\ddot{\mathbf{g}}^{f_\alpha} = \mathbf{0}, \quad \alpha = 1, ..., n_{\text{ec}} \tag{30b}$$

where $\mathbf{g}^{f_\alpha} = \left[\left(\mathbf{g}_{P_1}^{f_\alpha}\right)^T, \left(\mathbf{g}_{P_2}^{f_\alpha}\right)^T, ..., \left(\mathbf{g}_{P_{n^{\text{ph}}}}^{f_\alpha}\right)^T, \left(\mathbf{g}_{I_1}^{f_\alpha}\right)^T, \left(\mathbf{g}_{I_2}^{f_\alpha}\right)^T, ..., \left(\mathbf{g}_{I_{n^{\text{int}}}}^{f_\alpha}\right)^T\right]^T$, is the vector of the generalized degrees of freedom associated with the normal modes of the material phases and interfaces of the microstructure. The fine-scale nodal DOFs are recovered from the generalized DOFs using the transformation matrices:

$$\mathbf{d}^{f_\alpha} = \mathbf{T}^P \mathbf{T}^I \mathbf{g}^{f_\alpha} \tag{31}$$

Due to the periodic arrangement of unit cells, the model order reduction is performed only once for one unit cell and the same reduced stiffness and mass matrices are used for all unit cells. The global matrices and the force vector are assembled similarly as the full multiscale model in Section 3. The two-step model order reduction presented above significantly reduces the number of DOFs of the full spectral variational multiscale model and it is referred as reduced spectral variational multiscale (RSVM) model hereafter.

Another model order reduction strategy that can be used for reducing the fine-scale degrees of freedom is the unit cell based Craig-Bampton component mode synthesis (UCRSVM), which employs the unit cell normal modes as the reduced basis for the fine-scale problem, without distinguishing the material phases and interfaces and performing model order reduction to each of them. The fine-scale unit cell normal modes are obtained by solving the eigenvalue problem:

$$\left(\mathbf{K}^{f_\alpha f_\alpha} - \lambda^{f_\alpha}\mathbf{M}^{f_\alpha f_\alpha}\right)\boldsymbol{\phi}^{f_\alpha} = \mathbf{0} \tag{32}$$

Similar to RSVM, the normal mode matrix is constructed by truncating the higher frequency modes and the size of the stiffness and mass matrix is reduced by matrix transformation of the original matrices using the normal mode matrix (e.g., Eq. 25). It is observed that these modes do not well capture the wave propagation at the fine-scale. A comparison of UCRSVM to RSVM is provided in Section 6.2.

5 Implementation details

In this section, we provide implementation details of the proposed spectral variational multiscale model, including coarse-scale and fine-scale discretization, evaluation of element matrices, selection of the normal modes for reduced basis approximation, and time integration.

5.1 Multiscale discretization

The proposed multiscale approach has been verified on coarse-scale domains, where the domain of the coarse-scale element in the discretization conforms to that of a unit cell. The domain is first discretized using linear quadrilateral elements (the edges of the elements remain straight). Higher-order serendipity elements are then achieved by adding edge nodes and bubble nodes to the linear base element. The coordinates of the added nodes are linearly interpolated using the corner nodes of the linear base element. The node numbering and positioning in the cubic, quintic and septic elements are shown in Fig. 2. Each coarse-scale element is associated with the same unit cell morphology, which is meshed using the bilinear quadrilateral elements at the fine scale. In order to avoid numerical dispersion, sufficient

spectral order has to be employed for the coarse-scale element, and at least 10 elements have been used to resolve one wavelength at the fine scale. In a composite medium undergoing wave propagation at a given frequency, the softer material phases require more refinement, since the wave speed is slower and the wavelength is shorter in the softer material phases.

5.2 Element matrices

Construction of the appropriate element matrices requires numerical integration of the element matrices that involves fine-scale basis functions only (Eq. 17b), coarse-scale basis functions only (Eq. 17a) and the coupling terms with both coarse- and fine-scale basis functions (Eq. 17c). The integration of Eq. 17b for an arbitrary fine-scale element, Ω^e_α, is standard and performed using the Gaussian quadrature. The integration procedure for Eqs. 17a and c is non-standard and described below for the stiffness matrix in Eq. 17a. The mass matrix in Eqs. 17a and c are integrated in a similar fashion and skipped for brevity.

The integration of a function $f(\mathbf{x})$ over the fine-scale element domain is approximated as:

$$\int_{\Omega^e_\alpha} f(\mathbf{x})\ d\Omega^e_\alpha = \int_{\square^f} f\left(\mathbf{x}(\boldsymbol{\xi}^f)\right) J^f(\boldsymbol{\xi}) d\square^f \approx \sum_{l=1}^{n^f_{\text{int}}} f(\boldsymbol{\xi}^f_l) J^f(\boldsymbol{\xi}^f_l) W_l \tag{33}$$

where, $J^f = \det(\partial \mathbf{x}/\partial \boldsymbol{\xi}^f)$, is the fine-scale element Jacobian determinant and $\square^f$ is the fine-scale parent domain. n^f_{int} is the number of integration points to accurately evaluate the integrand. $\boldsymbol{\xi}^f_l$ and W_l are respectively the coordinates and weight of the integration point, l. In order to resolve the material heterogeneity within coarse-scale elements, each coarse-scale element is partitioned using the fine-scale mesh. The element stiffness matrix in Eq. 17a is expressed as:

$$\mathbf{K}^{cc}_\alpha = \int_{\Omega_\alpha} (\mathbf{B}^c_\alpha)^T \mathbf{C}(\mathbf{x}) \mathbf{B}^c_\alpha\ d\Omega_\alpha = \sum_{e=1}^{n_{\text{ef}}} \int_{\Omega^e_\alpha} (\mathbf{B}^c_\alpha)^T \mathbf{C}_e \mathbf{B}^c_\alpha\ d\Omega^e_\alpha \tag{34}$$

The evaluation of Eq. 34 using Eq. 33 requires the interpolated values of the spectral coarse-scale basis functions and their derivatives at the integration points within the fine-scale parent domain. The interpolated values are not readily available for the coarse-scale shape functions since they are defined in the coarse-scale parent domain, $\square^c$. In order to obtain the coarse-scale shape functions and their derivatives at the integration points within the fine-scale parent domain, a two-scale mapping procedure is employed.

Figure 4 schematically illustrates this mapping process for a cubic coarse-scale element. Let $\mathcal{M}^f$ and $\mathcal{M}^c$ respectively denote the fine-scale and coarse-scale isoparametric mappings that map functions defined in the fine-scale and coarse-scale parent domains to the physical domain. For any quadrature point within the fine-scale parent domain, its corresponding location in the

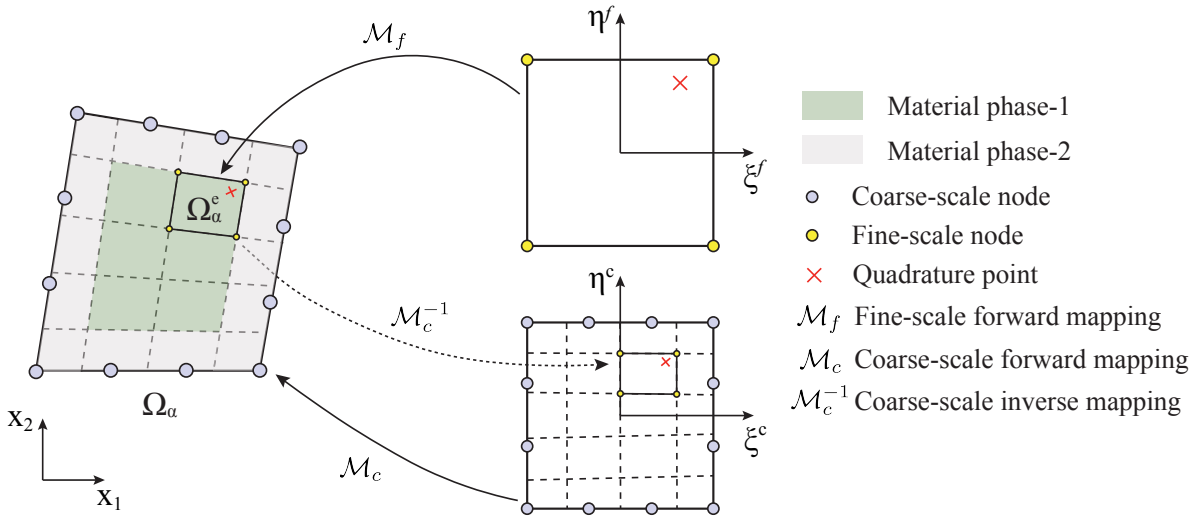

Figure 4: The two-scale element mapping relationship.

coarse-scale parent domain is obtained by first employing the fine-scale element isoparametric mapping to find its location in the physical domain, then applying the coarse-scale element inverse isoparametric mapping:

$$\boldsymbol{\xi}^c = \mathcal{M}_c^{-1}(\mathcal{M}_f(\boldsymbol{\xi}^f)) \tag{35}$$

where $\mathcal{M}_c^{-1}$ denotes the inverse mapping. The procedure of inverse mapping was originally proposed in Refs. [38, 39] and is elaborated in Appendix A. The inverse mapping for spectral elements is developed based on the theory of differential geometry and has been previously used in the context of distortion measures for 2D 8-node serendipity element and 3D hexahedron elements [69].

Gauss-Legendre quadrature rule is employed for numerical integration. Since linear quadrilateral element is used for the fine-scale discretization, integration of Eq. 17b is exact with 2×2 integration points. The number of integration points required to exactly evaluate Eqs. 17a and c depends on the spectral order of the coarse-scale shape functions. For a p^{th} order coarse-scale spectral element, the minimum number of integration points for Eqs. 17a and c are $(p+1)\times(p+1)$ and $(\frac{p}{2}+1)\times(\frac{p}{2}+1)$, respectively. For each integration point within the fine-scale parent domain, its corresponding location in the coarse-scale parent domain is obtained by Eq. 35. The coarse-scale shape functions and their derivatives are evaluated at this mapped point. Equation 17d that provides the force term at the coarse scale is integrated using the standard procedure over the coarse-scale element assuming that the boundary tractions remain unresolved at the fine scale.

5.3 Normal mode selection

The retained normal modes in the Craig-Bampton component mode synthesis and characteristic constraint mode reduction is typically selected by truncating the modes with higher natural frequencies [10, 8, 37]. The number of the normal modes is determined using a heuristic approach, based on ensuring that the desired accuracy is achieved with the resulting reduced order model. The appropriate number of material phase and interface normal modes used in RSVM are determined by gradually truncating the higher frequency modes, while evaluating the accuracy of the resulting transient response field compared to SVM. Parametric studies are provided in the next section for phononic crystals and acoustic metamaterials.

The general trend for the relation between wave frequency and the number of normal modes required for accuracy is that the required number of normal modes increases as the wave frequency increases. At low frequency, a few normal modes suffice to accurately predict wave propagation in the composite. As frequency increases, more modes need to be incorporated to retain accuracy, and the number of normal modes required for each material phase and interface varies depending on the constituent material properties.

Truncation of higher frequency modes is performed starting from the phase modes. Among all material phases, the normal modes of the stiff material phases are truncated first, since they have higher natural frequencies and typically only a few normal modes are important at the wave frequency of interest. The soft material phases require more normal modes to capture the deformation states during wave propagation, since their natural frequencies are lower than the stiff phases and more normal modes are excited. The interface normal modes of higher natural frequencies are truncated after the phase modes are selected. Since the reduced interface normal modes directly control the static deformation of adjacent material phases, the number of interface normal modes is chosen to be relatively large to accurately capture the static deformation of adjacent material phases. This relation is also observed in Refs. [8, 21] in the context of model order reduction of homogeneous structures. In the current study, the number of interface normal modes is selected such that it is larger than the smallest number of selected normal modes of adjacent material phases.

This heuristic way of mode selection can be improved by using a quantified metric that relates the number of modes for material phases and interfaces with the microstructure morphology, material properties and wave frequency. It requires a systematic study of the mode selection strategy for different phononic crystal and acoustic metamaterial designs and is beyond the scope of this manuscript.

5.4 Time integration

The monolithic time integration with Newmark's family of methods is employed in solving the discretized system of equations. In particular, we use the implicit unconditionally stable "Average acceleration" method [27]. Explicit time integration with lumped mass matrix is typically more efficient for wave propagation in homogeneous materials. In contrast, explicit integration for wave propagation in complex composites does not guarantee numerical efficiency over implicit methods, due to the large stiffness contrast between the constituents and variations in mesh size [20]. The time step size in the implicit time integration approach adopted herein is controlled by accuracy considerations only. Sufficiently fine time step size is used in the numerical examples below to resolve the temporal oscillations at each material point.

In the implicit time integration, inversion of global coefficient matrix $\mathbf{M}_{SVM} + \beta \Delta t^2 \mathbf{K}_{SVM}$ or $\mathbf{M}_{RSVM} + \beta \Delta t^2 \mathbf{K}_{RSVM}$ (β is the algorithmic parameter in the Newmark's method and Δt is the time step size) is performed at every time step. Since the coefficient matrix does not change during the time integration, it is decomposed only once before the time integration. A substitution is performed at each time step to update the solution.

6 Model verification

In this section, we assess the capability of SVM and RSVM in modeling transient wave propagation in periodic composites. Numerical examples of wave propagation in phononic crystals (PC) and acoustic metamaterials (AMM) are presented. The proposed model is verified against direct numerical simulations (DNS) using the finite element method where the full heterogeneous domain is resolved for a wide range of frequencies. The effects of coarse-scale element spectral order, material property contrast and the number of fine-scale normal modes on the accuracy and efficiency of the proposed model are discussed.

Figure 5(a) shows the two-dimensional unit cells of the acoustic metamaterial and phononic crystal that are used in the numerical examples. All examples are performed in plane strain condition. The acoustic metamaterial unit cell consists of three material phases: epoxy matrix, rubber coating and lead core. Under dynamic excitation, this material absorbs kinetic energy through locally resonant motion of the rubber coating and the lead core. This acoustic metamaterial design is originally proposed by Liu et al. [43] and has been analyzed using the computational homogenization framework [57]. In the current work, the dimensions of the unit cell, rubber coating and lead core, as well as the material properties of each phase are identical to those used in Ref. [43]. The phononic crystal unit cell is designed to have the same size as acoustic metamaterial unit cell. The steel inclusion has identical geometry as the lead core of

the acoustic metamaterial unit cell. The material properties of epoxy used for the phononic crystal are identical to those used for the acoustic metamaterial. The material properties used in the simulations are summarized in Table 1.

Table 1: Material properties used in simulations.

Material	Young's modulus (GPa)	Poisson's ratio	Density (kg/m^3)
Epoxy	3.6	0.3679	$1,180$
Rubber	11.8×10^{-5}	0.4688	$1,300$
Lead	40.8	0.3698	$11,600$
Steel	210	0.3	$7,900$

Each acoustic metamaterial unit cell is discretized using 2,752 linear quadrilateral elements and it contains 5,346 fine-scale DOFs. A fine mesh is used in the rubber coating phase with 10 elements in the radial direction in order to capture the resonant motion. The number of DOFs associated with the epoxy matrix, matrix-coating interface, rubber coating, coating-core interface and lead core are respectively 782, 256, 2,304, 256 and 1,748. The same mesh is used for the phononic crystal unit cell. The number of DOFs associated with epoxy matrix, matrix-inclusion interface and steel inclusion is respectively 3,342, 256 and 1,748. The proposed multiscale method leverage the periodic arrangement of unit cell discretization, therefore the element matrices are evaluated only for one unit cell and they are assembled block-by-block to construct the global matrices. In direct finite element simulations, each unit cell is discretized identically as the fine-scale discretization of the proposed multiscale method, i.e., 2,752 elements are used for each unit cell. Two composite structure configurations are investigated below, and transient sinusoidal velocity is applied for both cases, $\tilde{v}_x(t) = \sin(2\pi f t)$ m/s. The time step size is determined such that each loading cycle is resolved by 100 time steps: $\Delta t = 0.01/f$. It is verified that decreasing the time step size does not change the results significantly.

Both direct numerical simulations and the proposed model are excuted on a 4-core desktop with 2.3 GHz Intel processors and 16 GB of memory. In direct numerical simulations, the matrices of each element within each unit cell is computed and assembled. The time integration scheme and time step size are identical to the proposed multiscale method. For all simulations (DNS, SVM and RSVM), sparse matrix storage is used for the global matrices and sparse matrix Cholesky decomposition is applied to the global coefficient matrix.

6.1 Spectral variational multiscale model

In this section, we investigate wave propagation in the phononic crystal and acoustic metamaterial as shown in Fig. 5 using SVM. As explained previously, SVM constitutes the founda-

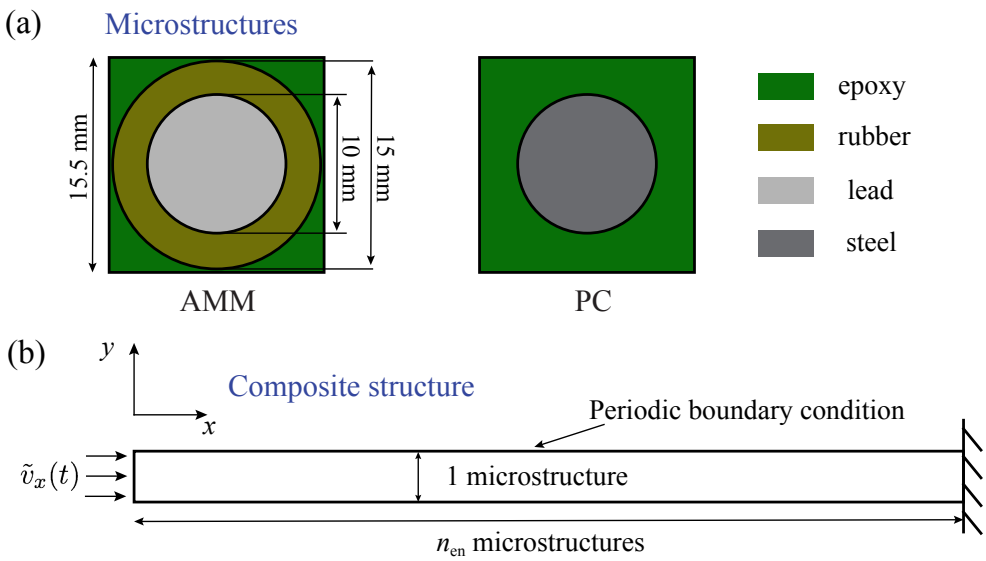

Figure 5: (a) Acoustic metamaterial and phononic crystal unit cells. (b) Composite structure and boundary conditions.

tion of RSVM, thus the numerical accuracy of SVM is examined for both acoustic metamaterials and phononic crytals. However, SVM does not offer computational efficiency compared to DNS, since they have similar number of degrees of freedom. The composite structure is composed of a row of n_{ec} microstructures. The right edge is fixed and the left edge is subject to sinusoidal velocity load, $\tilde{v}_x$. Periodic boundary condition is applied to the top and bottom edges. n_{ec} is 50 for acoustic metamaterial and 20 for phononic crystal examples. The simulation time is $T = 1/f$ s for acoustic metamaterial and $T = 1.5 \times 10^{-4}$ s for phononic crystal examples. The simulation setup for the acoustic metamaterial example is identical to that used in Ref. [57].

6.1.1 Accuracy of SVM at various wave frequencies

Figure 6 shows the velocity profiles along the bottom edge of the phononic crystal structure at time $t = T$ as predicted by SVM and the reference simulations. The vertical axis label v_x denotes the measured velocity in x direction. The responses at the applied frequencies of 10, 50, 100, 140 kHz are shown. The frequencies are respectively in the first pass band, the first stop band, the second pass band and the second stop band. For all applied loading frequencies, SVM very accurately captures the wave field, including wave dispersion in the acoustic regime (10 kHz), wave attenuation in the stop bands (50 kHz and 140 kHz) and wave amplification in the optical regime (100 kHz). Within the second stop band ($f = 140$ kHz), the wavelength is shorter than the microstructure. Since the present approach does not rely on the assumption of separation of scales, the short wavelength response is accurately captured. The

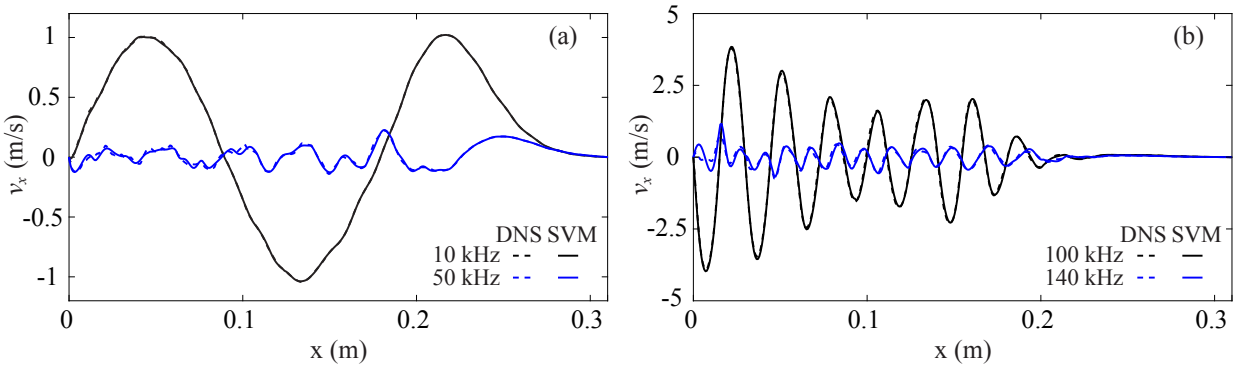

Figure 6: Velocity profiles as predicted by SVM and reference simulations along the bottom edge of the PC structure at $t = T$: (a) 10 and 50 kHz, (b) 100 and 140 kHz.

lateral velocity contours within the phononic crystal for the aforementioned four frequencies are shown in Fig. 7. In the first pass band, the wave propagates through both the matrix and inclusion with similar amplitudes. In contrast, the wave appears to propagate through the matrix only when its frequency is within the second pass band. While both the first and second stop bands feature a significant reduction in wave amplitude, the distribution of the kinetic energy density within the phases is different. The kinetic energy is concentrated in the inclusion within the first stop band, whereas it is concentrated in the matrix when the wave frequency is within the second stop band. SVM accurately predicts the wave patterns at all four frequency regimes.

Figure 8 shows the velocity profiles along the bottom edge of the structure when acoustic metamaterial unit cell is used. Compared to the phononic crystal, wave attenuation occurs at much lower frequencies in the acoustic metamaterial. At these frequencies, the wavelength is much larger than the size of microstructures. The mechanism of wave attenuation is the local resonance. As shown in Fig. 9, the local resonance is mainly due to the resonant motion of the lead core at $f = 500$ Hz. As the wave frequency increases, a transition from the core resonance to the coating resonance occurs ($f = 700$ Hz). At $f = 1,300$ Hz, the coating resonance becomes dominant. This observation is consistent with Ref. [43]. The local resonance becomes weaker as the wave frequency further increases ($f = 2,700$ Hz). The rubber-coated lead inclusion behaves more like a soft scatterer than a resonator and less kinetic energy is absorbed in the lead core and the rubber coating. As a consequence, the wave amplitude increases at high frequencies as shown in Fig. 8(b).

The transmitted wave amplitude spectra for the phononic crystal and acoustic metamaterial are shown in Fig. 10. The spectra are built based on wave amplitudes measured along the bottom edge of the composite structure (Fig. 5(b)) at $t = T$. Along the measurement line (i.e., the bottom edge), the maximum amplitude of the velocity field is employed for the acoustic

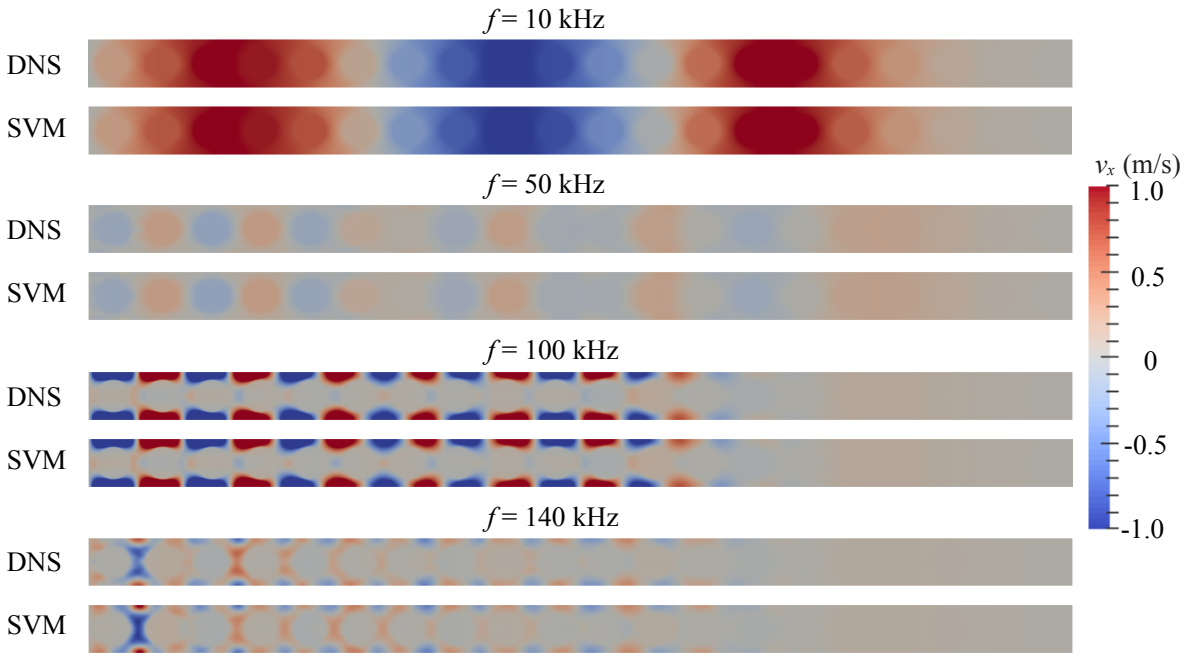

Figure 7: Velocity contours of the PC structure as predicted by SVM and reference simulations at $t = T$.

metamaterial spectrum, whereas the maximum amplitude of the velocity field 5 unit cells away from the loaded end is used for the phononic crystal spectrum. The probed frequency range covers up to the third pass band for the phononic crystal and the pass band beyond the local resonance stop band for the acoustic metamaterial. For wave propagation in the phononic crystal (Fig. 10(a)), SVM accurately captures the transmission spectrum up to the second stop band. The accuracy decreases as the wave frequency increases. In the third pass band, the wavelength is much shorter than the length of the unit cell. The septic shape functions used at the coarse scale does not provide sufficient resolution to accurately capture the wave field, and the error is therefore larger in this regime. For wave propagation in the acoustic metamaterial (Fig. 10(b)), SVM is accurate in the entire range of probed frequencies.

6.1.2 Parametric study for accuracy assessment

A parametric study is performed to examine the accuracy of SVM as a function of the spectral order of the coarse-scale shape functions. Figure 11 compares the velocity field obtained using SVM with spectral coarse-scale elements of different orders with the reference simulations. The composite structure made of phononic crystal unit cells is considered in this study. The structure is excited at two frequencies. At $f = 10$ kHz, the wavelength is about 12 times of the size of a coarse-scale element. A slight numerical dispersion is observed when linear elements are used. Simulations with higher-order spectral elements agree very well with

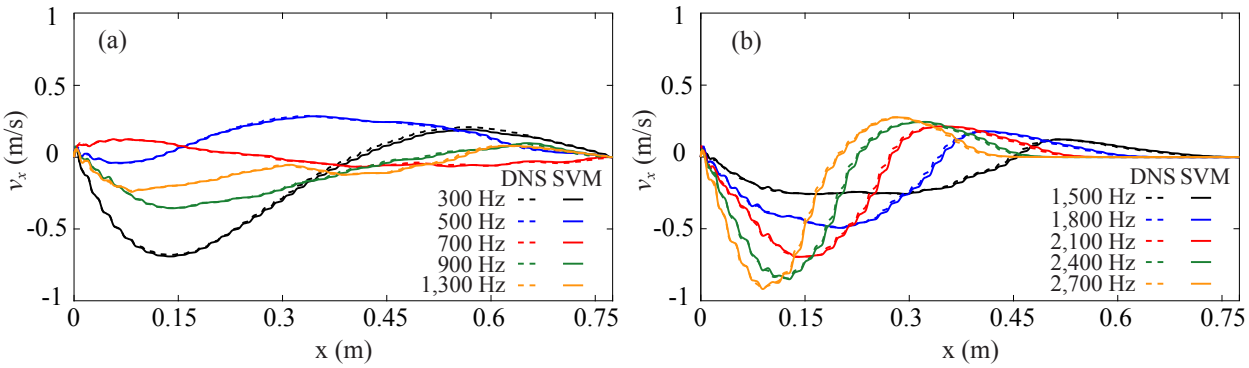

Figure 8: Velocity profiles as predicted by SVM and reference simulations along the bottom edge of the AMM structure at $t = T$: (a) 300, 500, 700, 900 and 1,300 Hz, (b) 1,500, 1,800, 2,100, 2,400 and 2,700 Hz.

the reference simulations. At $f = 100$ kHz, linear coarse-scale element fails to capture the propagation of the high frequency wave, and a significant phase shift is observed for cubic element. Quintic and septic coarse-scale elements accurately capture the wave field. This observation confirms the importance of using higher-order spectral elements at the coarse scale to capture the high frequency waves using the proposed multiscale approach.

Similar to the observations for phononic crystals, the accuracy of SVM requires sufficiently high order spectral coarse-scale elements in modeling acoustic metamaterials. Figure 12 shows the velocity profiles predicted by SVM with varying orders of coarse-scale elements compared with the reference simulations under two loading frequencies. The figure demonstrates convergence to the reference simulations as the order of the coarse-scale elements is increased. At $f = 300$ Hz and $f = 2,000$ Hz, the wavelength within the epoxy matrix is much larger compared to the size of coarse-scale element. However, the velocity profiles predicted by models using linear and cubic elements show significant discrepancy. This is attributed to the observation that the wavelength within the rubber coating is much shorter than it is in the epoxy matrix, and these short waves could not be accurately captured using low-order elements.

Next, we assess the accuracy of the proposed multiscale approach in capturing the transient dynamic response within the composite domain as a function of contrast in the constituent elastic moduli. Figure 13 shows the velocity profiles as predicted by SVM and reference simulations for various Young's modulus contrasts. The parametric study is performed by varying the Young's modulus ratio by 0.1 times ($r_E = 5.83$ for PC and $r_E = 3.5 \times 10^4$ for AMM) or 10 times ($r_E = 583$ for PC and $r_E = 3.5 \times 10^6$ for AMM) compared to the Young's modulus ratio used in previous examples ($r_E = 58.3$ for PC and $r_E = 3.5 \times 10^5$ for AMM). Varying Young's modulus contrast is achieved by varying the Young's modulus of epoxy for phononic crystals and rubber for acoustic metamaterials, while other material properties

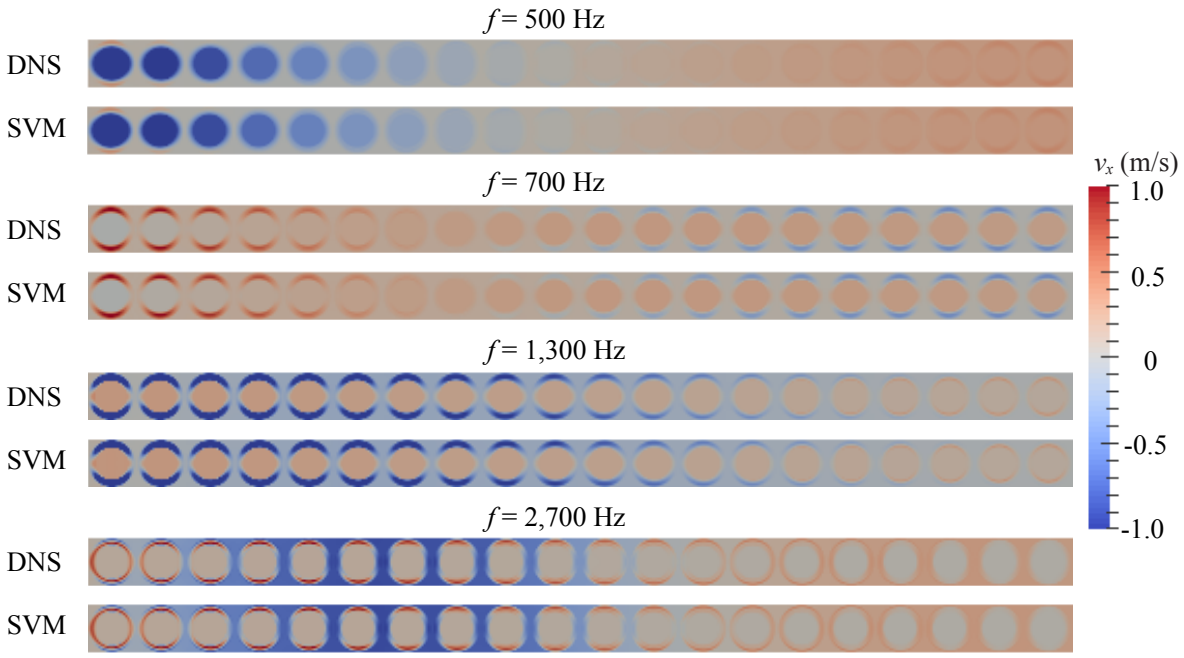

Figure 9: Velocity contours of the AMM structure as predicted by SVM and reference simulations at $t = T$.

remain unchanged. In the phononic crystal case (Fig. 13(a)), a change in the Young's modulus of the matrix constituents results in a significant change in the length of the propagating wave when excited with a frequency of 20 kHz. Compared to $r_E = 58.3$, increasing the modulus ratio by decreasing the modulus of the matrix leads to shorter wavelength, resulting in strong destructive interactions and stop band formation when $r_E = 583$. When the acoustic metamaterial is excited at $f = 2,000$ Hz, the wavelength remains nearly unchanged when the modulus of the coating is decreased 10 times. Contrary to the strong attenuation observed in the phononic crystal, increasing the modulus contrast results in weaker attenuation. This is because the stop band shifts to lower frequencies due to the decreased coating modulus. The loading frequency is further away from the stop band. On the other hand, reducing the modulus contrast leads to stronger attenuation at $f = 2,000$ Hz, as the frequency range for the stop band is shifted to higher frequencies and $f = 2,000$ Hz falls in the stop band.

6.2 Reduced order spectral variational multiscale model

In this section, we investigate the accuracy and numerical efficiency of the proposed reduced order spectral multiscale model for wave propagation in the phononic crystal and acoustic metamaterial. The geometry, boundary and loading conditions for the numerical example are identical to those described in Section 6.1. Septic coarse-scale basis functions are employed for

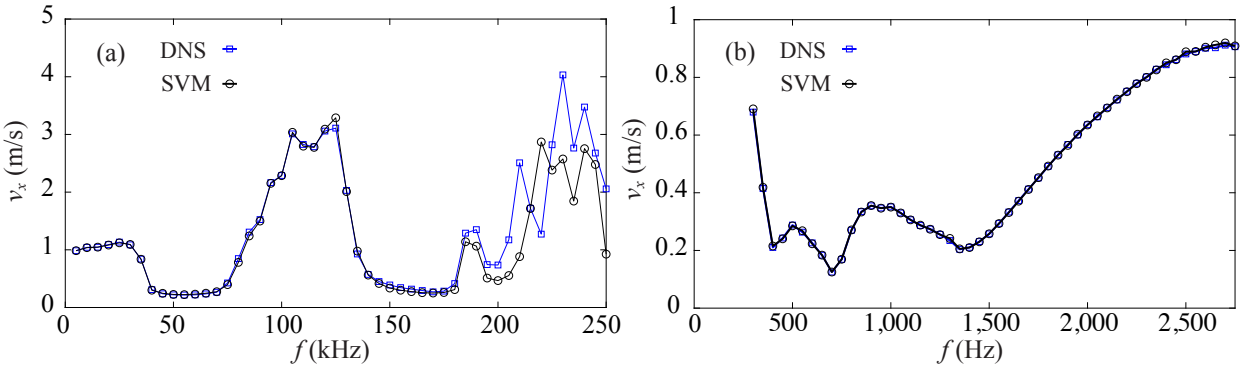

Figure 10: Transmitted wave amplitude spectra for (a) phononic crystal, and (b) acoustic metamaterial.

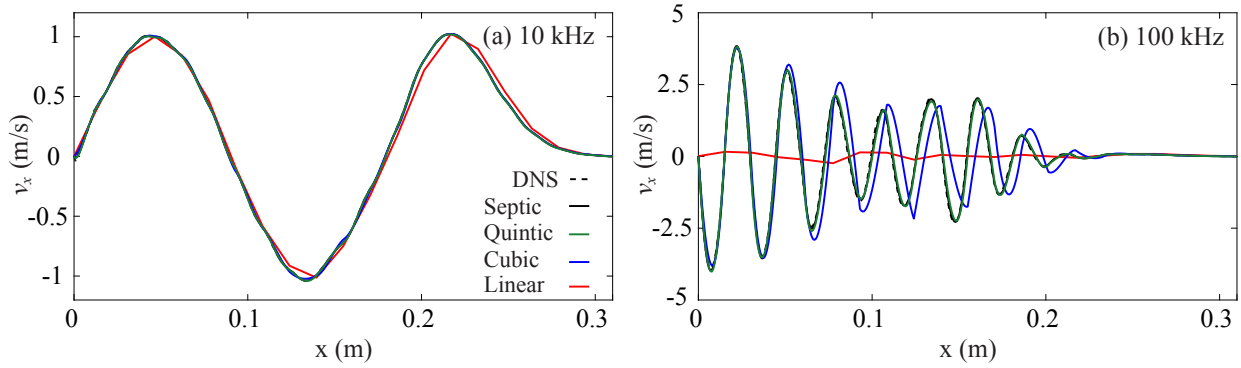

Figure 11: The effect of the spectral order of coarse-scale element on the accuracy of SVM for the phononic crystal structure simulation: (a) $f = 10$ kHz, and (b) $f = 100$ kHz.

RSVM.

Figure 14 shows the velocity profiles along the bottom edge of the phononic crystal evaluated using RSVM compared to reference simulations and UCRSVM. The selected number of normal modes for RSVM are 20, 40, 80, 160. The numbers of selected modes for matrix, matrix-inclusion interface and inclusion are respectively 5-10-5, 10-20-10, 20-40-20 and 40-80-40. UCRSVM incorporates the first 320 unit cell normal modes. The frequency of the highest selected mode is about 10 times of the maximum frequency of interest for both PC and AMM. In the first pass band (Fig. 14(a)), RSVM agrees well with the reference simulations using as few as 40 modes. Using fewer modes results in a slight phase shift. Even with significantly larger number of modes, UCRSVM does not capture the wave field as accurately. As the wave frequency increases, the wavelength becomes shorter, and additional modes are required to capture the wave field with similar accuracy. At $f = 50$ kHz (the first stop band), 40 modes are not sufficient to accurately capture the wave field. RSVM with 80 modes agrees well with the reference simulations. At higher frequencies, in the second pass band and second stop

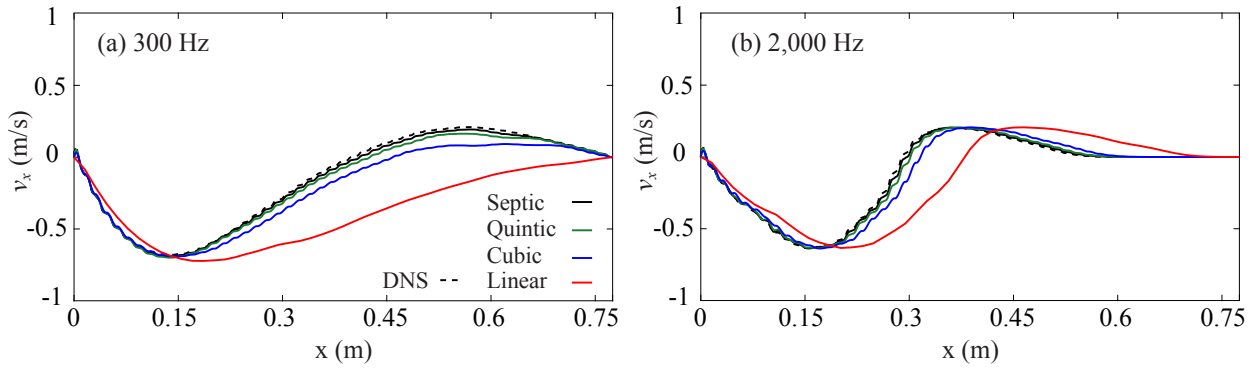

Figure 12: The effect of the spectral order of coarse-scale element on the accuracy of SVM for the acoustic metamaterial simulation: (a) $f = 300$ Hz, and (b) $f = 2,000$ Hz.

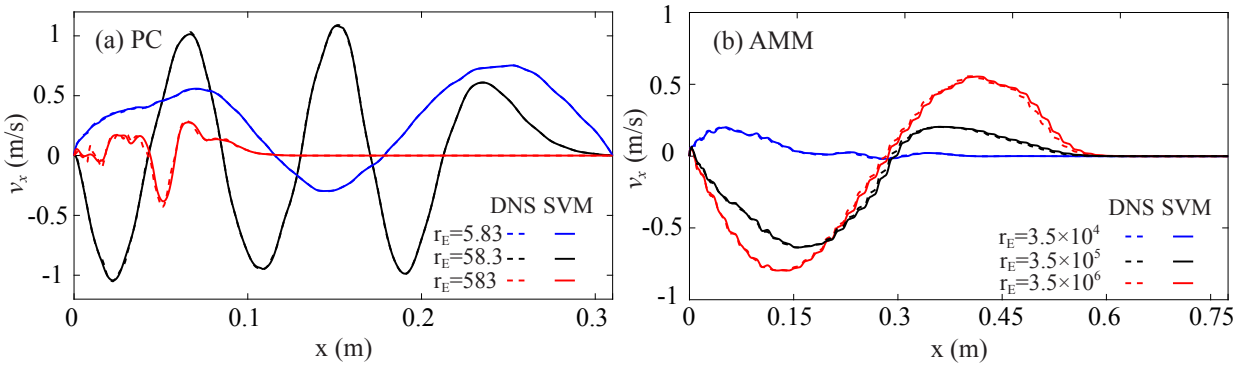

Figure 13: The effect of the material property contrast on the accuracy of SVM: (a) PC at $f = 20$ kHz, (b) AMM at $f = 2,000$ Hz.

band, while RSVM with 80 and 160 modes both predict the short wavelength responses, it is apparent that more retained modes result in better accuracy. The computational efficiency decreases as the number of modes increases. It is important to note that due to the high modulus contrast between epoxy and steel, the critical time step size for explicit time integration is approximately 3.6×10^{-9} s. Using vectorized explicit time integration for reference simulations in fact is more computationally expensive than the implicit time integration.

Figure 15 shows the velocity profiles as predicted using RSVM with 80, 160 and 320 modes, compared to reference simulations and UCRSVM for the acoustic metamaterial. The numbers of modes for the epoxy matrix, matrix-coating interface, rubber coating, coating-core interface and lead core are respectively 10-20-30-10-10, 20-40-70-20-10 and 20-100-150-40-10. The number of modes selected for the lead core is much smaller than the others since it undergoes primarily rigid body motion due to high density and modulus compared to the soft rubber coating. The wave within the epoxy matrix can also be well captured with relatively small number of modes, because the wavelength within the epoxy matrix is much larger than the

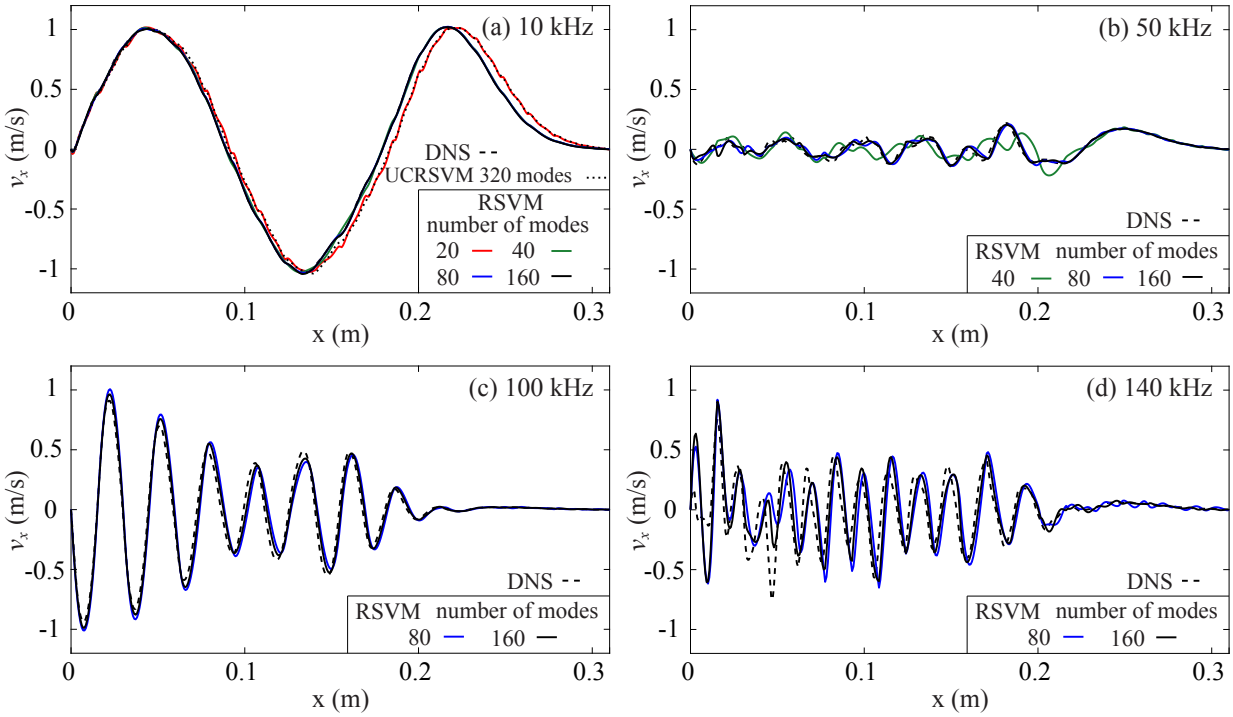

Figure 14: Velocity profiles as predicted by RSVM with different number of modes and reference simulations along the bottom edge of the PC structure at $t = T$: (a) 10 kHz, (b) 50 kHz, (c) 100 kHz, (d) 140 kHz.

size of the unit cell in the frequency range of interest. The rubber coating requires significant number of modes to accurately capture its deformation since higher natural modes of vibration can be easily excited even at low frequency. As the number of selected modes increases, more modes are incorporated for the rubber coating and the adjacent interfaces, while the numbers of modes for the epoxy matrix and lead core remains unchanged. The number of modes for the rubber coating is approximately 1.5 and 3 to 4 times the numbers of modes for the coating-core interface and matrix-coating interface, respectively. The latter interface retains more modes because more modes are selected for the epoxy matrix than the lead core. Figure 15 shows that the accuracy of RSVM improves with increasing number of modes. Compared to the phononic crystal example, modeling acoustic metamaterial requires more modes to accurately predict the wave field. This is due to the more complex unit cell architecture with more phases and interfaces, and the presence of the soft rubber phase that requires a large number of modes to resolve its deformation. The UCRSVM approach exhibits significant discrepancy even with a large number of modes (800). This implies that the unit cell normal modes with homogeneous boundaries are not proper basis for the fine-scale problem for the proposed multiscale formulation, and justifies the phase mode synthesis strategy.

Figure 16 shows the velocity history of the middle point in vertical direction of phononic

crystal and acoustic metamaterial structures at $x = 0.155\ m$ with different Young's modulus contrasts at different frequencies. SVM and RSVM are compared to DNS, in order to examine the effects of using homogeneous Dirichlet boundary condition at the fine-scale and the material-phase-based model order reduction. Comparing respectively Fig. 16(a) with (b), (c) with (d), (e) with (f), and (g) with (h), it is observed that as the wave frequency increases, the accuracy of SVM and RSVM decreases. In addition, higher material property contrast leads to higher error, comparing Fig. 16(d) with (b), and Fig. 16(h) with (f), respectively. This observation reveals that the error introduced by the assumptions of homogeneous Dirichlet boundary condition at the fine-scale and material-phase-based mode synthesis increases as wave frequency and material property contrast increase.

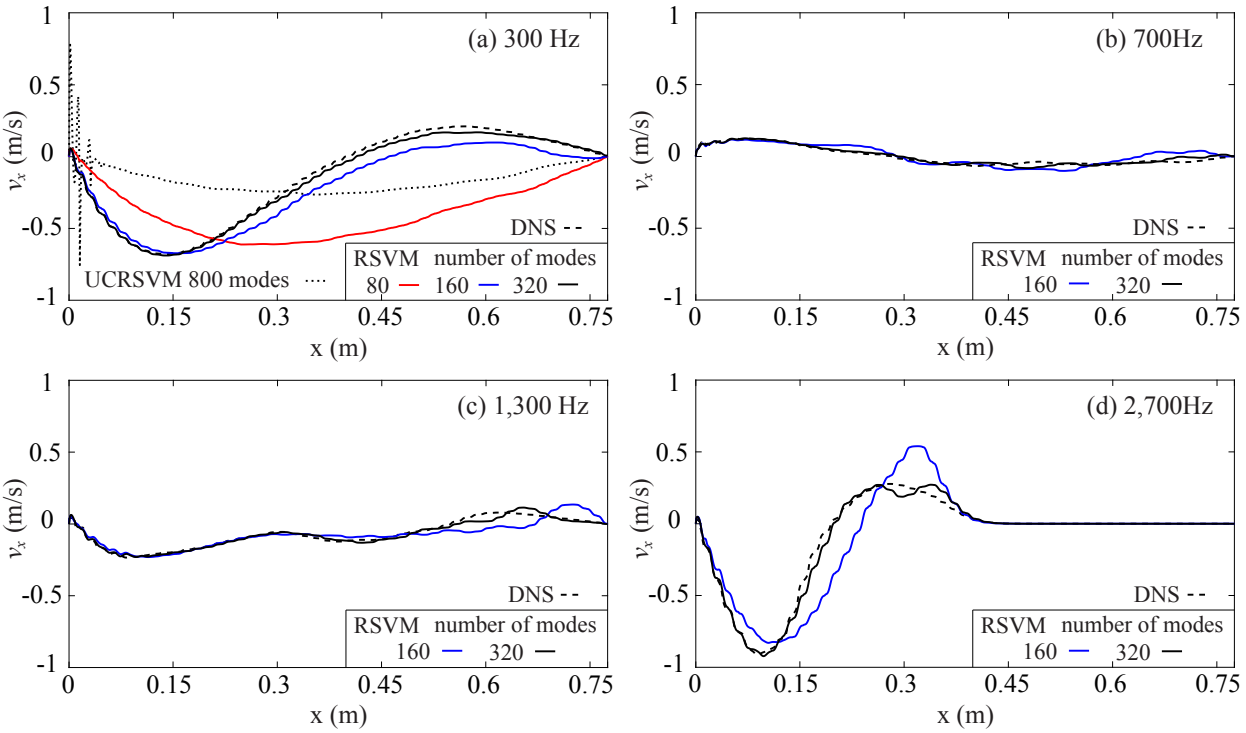

Figure 15: Velocity profiles as predicted by RSVM with different number of modes and reference simulations along the bottom edge of the AMM structure at $t = T$: (a) 300 Hz, (b) 700 Hz, (c) 1,300 Hz, (d) 2,700 Hz

The computational efficiency of the example in Fig. 15(a) is shown in Table 2. the normalized computation time indicates the computation time of RSVM divided by the computation time of the reference simulation during the preprocessing and time integration. The preprocessing step includes element matrices evaluation and global matrices assembly for the reference simulation, and element matrices evaluation at both scales, fine-scale model basis reduction and global matrices assembly for RSVM. Significant computational efficiency is achieved at

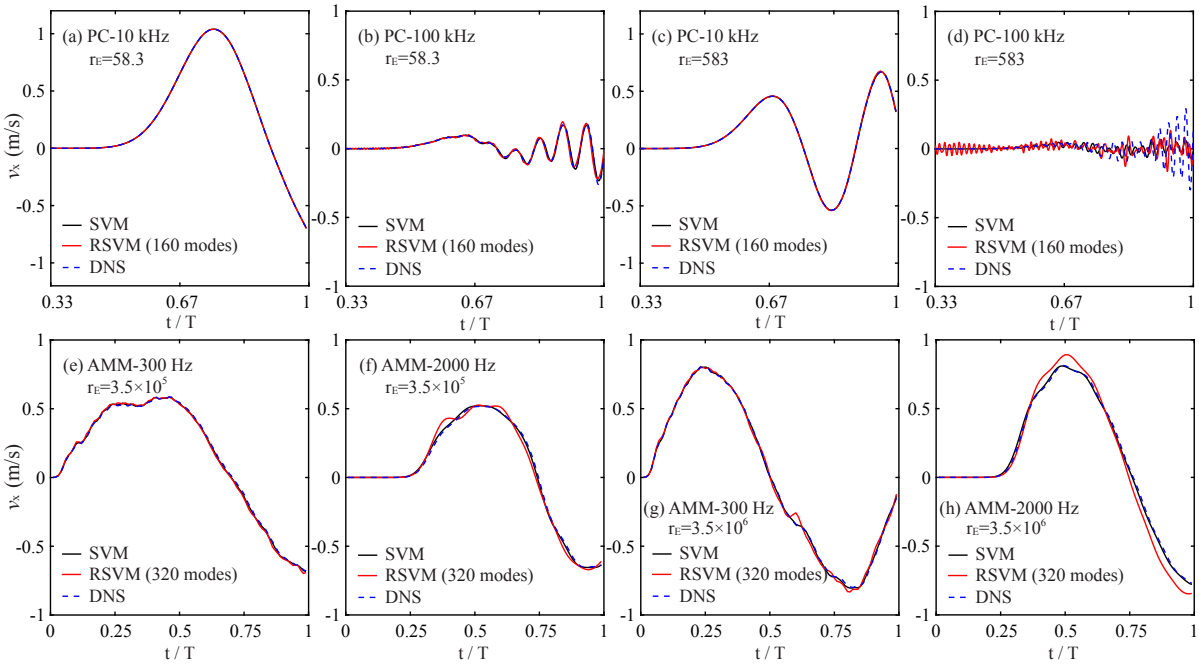

Figure 16: Velocity history of the middle point of vertical unit cell boundary at $x = 0.155\ m$ for phononic crystals and acoustic metamaterials with different Young's modulus contrasts at different frequencies: (a) PC at 10 kHz with $r_E = 58.3$, (b) PC at 100 kHz with $r_E = 58.3$, (c) PC at 10 kHz with $r_E = 583$, (d) PC at 100 kHz with $r_E = 583$, (e) AMM at 300 Hz with $r_E = 3.5 \times 10^5$, (f) AMM at 2000 Hz with $r_E = 3.5 \times 10^5$, (g) AMM at 300 Hz with $r_E = 3.5 \times 10^6$, (h) AMM at 2000 Hz with $r_E = 3.5 \times 10^6$.

both preprocessing and time integration steps. As more modes are incorporated, the computation time remains nearly unchanged in preprocessing, and increases in time integration. For preprocessing, the efficiency is mainly attributed to that the coarse- and fine-scale element matrices are evaluated only once for one unit cell and the block-by-block global matrices assembly. The computational efficiency of RSVM in time integration is achieved due to the reduced global matrices size compared to reference simulations.

Table 2: Normalized computation time of RSVM for the AMM structure simulation.

Number of modes	Preprocessing	Time integration
80	0.343	0.034
160	0.345	0.082
320	0.349	0.185

6.3 Elastic waveguide simulation using RSVM

In this section, we investigate the transient wave propagation in an elastic waveguide shown in Fig. 17. The length and height of the structure are 15 unit cells and 12 unit cells, respectively. The waveguide is constructed as the periodic arrangement of the phononic crystal unit cell (Fig. 5), except along an elbow path made of homogeneous epoxy. This design has been previously investigated experimentally and numerically in the context of acoustic wave guiding [36] in water using periodic array of steel cylinders. The right boundary of the waveguide is fixed and sinusoidal velocity is applied along the left boundary. The total simulation time is $T = 4 \times 10^{-4}$ s.

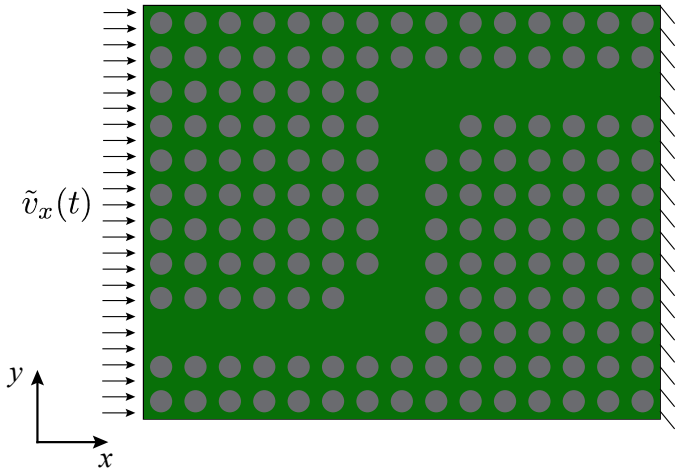

Figure 17: The geometry and boundary conditions of the elastic waveguide simulation.

The discretization for the phononic crystal unit cell is identical to the previous sections for both DNS and RSVM. In reference simulations, 495,360 elements are used to discretize the domain. In multiscale simulations, the elements within the homogeneous path region are not enriched with the fine-scale problem, but are discretized using the septic coarse-scale shape functions. 80 modes are incorporated as the fine-scale basis and the number of modes for epoxy matrix, interface and steel inclusion are respectively 20, 40 and 20. The total numbers of DOFs for DNS and RSVM are respectively 991,439 and 21,605.

Figure 18 shows the velocity contours of wave propagation in the composite structure. Sinusoidal velocity at a frequency of $f = 10$ kHz is applied to the left boundary and the snapshots are taken at 4 separate time instances. The elastic wave travels through the entire composite structure and forms a complex wave pattern due to reflections at the structural boundaries. The dispersion induced by the microstructures is relatively minor, because the macroscopic wavelength is significantly larger than the size of the microstructure. When the wave frequency is increased to 60 kHz, the frequency falls within the first stop band (Fig. 10).

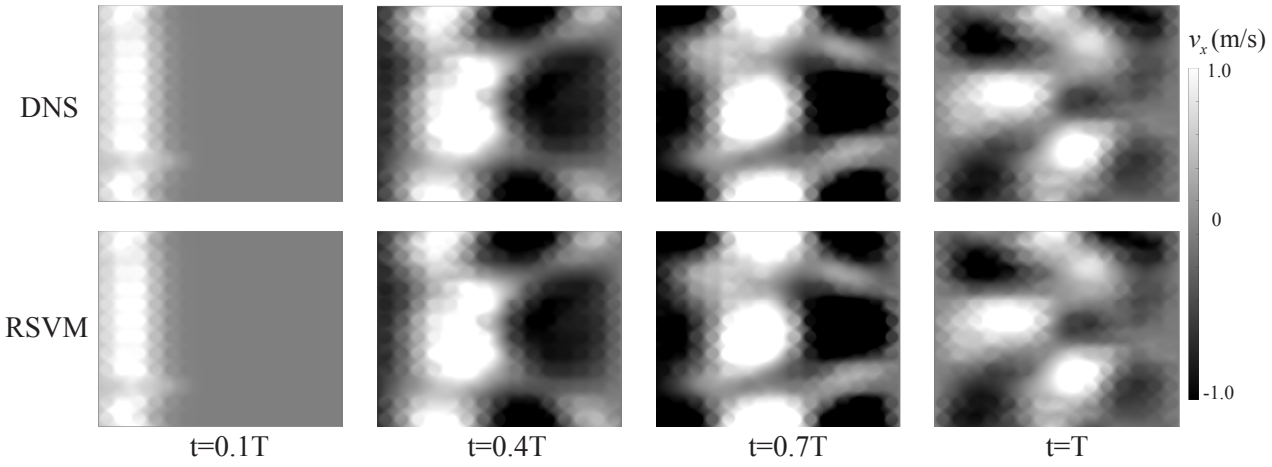

Figure 18: Velocity contours of wave propagation in elastic waveguide, $f = 10$ kHz.

At this frequency, the wavelength is approximately twice of the unit cell size, resulting in significant destructive interactions within the composite structure. Because of the stop band formation, the elastic wave is only permitted to propagate within the homogeneous guide, as shown in Fig. 19. The wave amplitude outside of the guide is strongly attenuated and is much lower than it is within the guide. At both of these frequencies, it is observed that RSVM with 80 modes accurately captures the overall wave field.

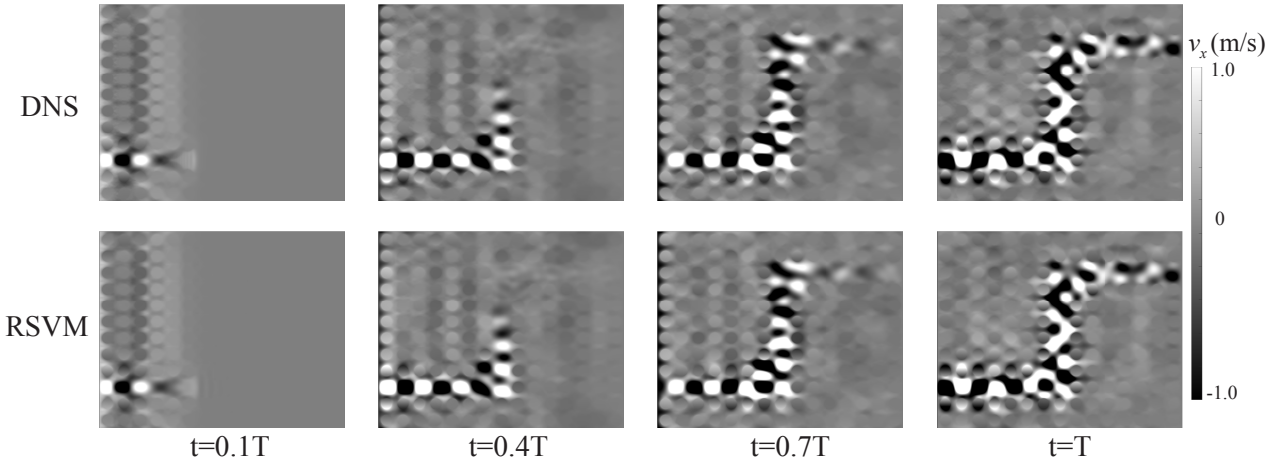

Figure 19: Velocity contours of wave propagation in elastic waveguide, $f = 60$ kHz.

The computation time for DNS and RSVM in preprocessing and time integration is shown in Table 3. Similar to the acoustic metamaterial case shown in Table 2, RSVM is significantly faster than DNS in both preprocessing and time integration. In the present numerical example, since a relatively short period of time is simulated, the time integration is less computationally expensive than the preprocessing. The computation time of time integration linearly increases as longer total simulation time is investigated.

Table 3: Computation time in the phononic crystal waveguide simulation.

Simulation model	Preprocessing	Time integration
DNS	9.5 hours	765.7 seconds
RSVM	0.5 hours	4.7 seconds

7 Conclusion

This manuscript presented a spectral variational multiscale model for transient wave propagation in phononic crystals and acoustic metamaterials. The proposed model is developed based on the variational multiscale enrichment method, employing the additive split of the solution field and numerically evaluating the coupled system of equations at two scales. Spectral elements are employed at the coarse scale to accurately resolve the wave field. A material-phase-based model order reduction method is proposed for efficient evaluation of the fine-scale numerical solution. Based on the Craig-Bampton component mode synthesis and the characteristic constraint mode reduction, the proposed approach distinguishes material phases and interfaces at the fine scale and perform modal reduction individually.

A novel contribution of the proposed model is that it does not introduce drastic accuracy reduction in composites with high material property contrast and it does not employ the scale separation principle. This permits the proposed model to accurately capture wave propagation in both phononic crystals and acoustic metamaterials over a wide frequency range. The accuracy and computational efficiency of the spectral variational multiscale model is demonstrated for both phononic crystals and acoustic metamaterials. It is shown that the wave field in the phononic crystal is accurately predicted by the proposed model up to the second stop band, where the wavelength is shorter than the microstructure. The proposed model well captures the local resonance and wave attenuation in acoustic metamaterials. Computational cost reduction is achieved in both preprocessing and time integration for the reduced order model. The computational efficiency decreases as the number of incorporated modes increases. It is observed that more modes are required to accurately capture the wave field in acoustic metamaterials than phononic crystals, due to the increased number of modes to resolve the soft material phase and adjacent interfaces.

In the near future, the current model will be extended to 3D for more general applications in design and analysis of phononic crystals and acoustic metamaterials. Furthermore, a broader range of material constitutive behaviors need to be investigated, including the viscoelasticity and thermal effect [26], in order to explore undiscovered design space for exotic dynamic properties of architectured composites. The proposed model can also be formulated in frequency domain for steady-state wave propagation, which is frequently employed to in-

vestigate the response of complex architectured composites at a single frequency [51]. From the computational perspective, the use of other fine-scale boundary conditions (e.g., periodic boundary condition) and modal basis functions will be investigated for improved accuracy and computational efficiency.

Acknowledgment

The authors gratefully acknowledge the financial support of the National Science Foundation, CMMI Mechanics of Materials and Structures Program, and the Computational and Data Enabled Science and Engineering (CDS&E) program (Grant No.: 1435115).

Appendix A Inverse isoparametric mapping

This appendix provides the detailed procedure of the inverse isoparametric mapping for 2D quadrilateral elements. The procedure is developed based on Ref. [39] that maps any point within the coarse-scale element in Cartesian coordinates to the isoparametric coordinates.

The inverse isoparametric mapping for a higher order element is performed based on its cord element, which is the 4-node linear quadrilateral element that is formed by the corner nodes of the quadrilateral, i.e., node $1, 2, 3, 4$ in Fig. 2. The isoparametric mapping for the cord element is expressed as:

$$\begin{Bmatrix} x \\ y \end{Bmatrix} = \begin{Bmatrix} a_0 + a_1\xi + a_2\xi\eta + a_3\eta \\ b_0 + b_1\xi + b_2\xi\eta + b_3\eta \end{Bmatrix} \tag{A.1}$$

where,

$$\begin{aligned} a_0 &= \frac{1}{4}(x_1 + x_2 + x_3 + x_4); \quad b_0 = \frac{1}{4}(y_1 + y_2 + y_3 + y_4) \\ a_1 &= \frac{1}{4}(-x_1 + x_2 + x_3 - x_4); \quad b_1 = \frac{1}{4}(-y_1 + y_2 + y_3 - y_4) \\ a_2 &= \frac{1}{4}(x_1 - x_2 + x_3 - x_4); \quad b_2 = \frac{1}{4}(y_1 - y_2 + y_3 - y_4) \\ a_3 &= \frac{1}{4}(-x_1 - x_2 + x_3 + x_4); \quad b_3 = \frac{1}{4}(-y_1 - y_2 + y_3 + y_4) \end{aligned} \tag{A.2}$$

Following the formula provided in Ref. [39], the geodesic parameters are written as:

$$\begin{aligned} \xi^g &= \bar{\xi} - \gamma\bar{\xi}\bar{\eta} + (\alpha\gamma\bar{\xi}^2\bar{\eta} + \gamma^2\bar{\xi}\bar{\eta}^2) - (\alpha^2\gamma\bar{\xi}^3\bar{\eta} + 2\alpha\gamma^2\bar{\xi}^2\bar{\eta}^2 + \gamma^3\bar{\xi}\bar{\eta}^3) \\ \eta^g &= \bar{\eta} - \alpha\bar{\xi}\bar{\eta} + (\alpha^2\bar{\xi}^2\bar{\eta} + \alpha\gamma\bar{\xi}\bar{\eta}^2) - (\alpha^3\bar{\xi}^3\bar{\eta} + 2\alpha^2\gamma\bar{\xi}^2\bar{\eta}^2 + \alpha\gamma^2\bar{\xi}\bar{\eta}^3) \end{aligned} \tag{A.3}$$

where,

$$\begin{Bmatrix} \bar{\xi} \\ \bar{\eta} \end{Bmatrix} = \frac{1}{J_0} \begin{bmatrix} b_3 & -a_3 \\ -b_1 & a_1 \end{bmatrix} \begin{Bmatrix} x \\ y \end{Bmatrix} \tag{A.4}$$

The parameters are:

$$\begin{aligned} J_0 &= a_1 b_3 - a_3 b_1 \\ \alpha &= (a_1 b_2 - a_2 b_1)/J_0 \\ \gamma &= (a_2 b_3 - a_3 b_2)/J_0 \end{aligned} \tag{A.5}$$

A linear mapping is then performed to map the geodesic parameters to the isoparametric

variables:

$$\begin{Bmatrix} \xi \\ \eta \end{Bmatrix} = \begin{Bmatrix} \hat{a}_0 + \hat{a}_1\xi^g + \hat{a}_2\xi^g\eta^g + \hat{a}_3\eta^g \\ \hat{b}_0 + \hat{b}_1\xi^g + \hat{b}_2\xi^g\eta^g + \hat{b}_3\eta^g \end{Bmatrix} \tag{A.6}$$

where, $\hat{a}_i$ and $\hat{b}_i$, $i = 1, 2, 3, 4$, are computed using Eq. A.2 with (x_i, y_i) taken as: $(-1, -1)$, $(-1, 1)$, $(1, 1)$ and $(-1, 1)$, respectively.

References

[1] T. Arbogast. Implementation of a locally conservative numerical subgrid upscaling scheme for two-phase darcy flow. *Comput. Geosci.*, 6:453–481, 2002.

[2] B. V. Asokan and N. Zabaras. A stochastic variational multiscale method for diffusion in heterogeneous random media. *J. Comput. Phys.*, 218:654–676, 2006.

[3] I. Babuška and M. Suri. The p-and hp versions of the finite element method, an overview. *Comput. Methods Appl. Mech. Eng.*, 80:5–26, 1990.

[4] C. Boutin and J. L. Auriault. Rayleigh scattering in elastic composite materials. *Int. J. Eng. Sci.*, 31:1669–1689, 1993.

[5] S. Brûlé, E. H. Javelaud, S. Enoch, and S. Guenneau. Experiments on seismic metamaterials: molding surface waves. *Phys. Rev. Lett.*, 112:133901, 2014.

[6] F. Casadei, J. J. Rimoli, and M. Ruzzene. A geometric multiscale finite element method for the dynamic analysis of heterogeneous solids. *Comput. Methods Appl. Mech. Eng.*, 263:56–70, 2013.

[7] F. Casadei, J. J. Rimoli, and M. Ruzzene. Multiscale finite element analysis of wave propagation in periodic solids. *Finite Elem. Anal. Des.*, 108:81–95, 2016.

[8] M. P. Castanier, Y. C. Tan, and C. Pierre. Characteristic constraint modes for component mode synthesis. *AIAA journal*, 39:1182–1187, 2001.

[9] A. Colombi, P. Roux, S. Guenneau, P. Gueguen, and R. V. Craster. Forests as a natural seismic metamaterial: Rayleigh wave bandgaps induced by local resonances. *Sci. Rep.*, 6:19238, 2016.

[10] R. Craig and M. Bampton. Coupling of substructures for dynamic analyses. *AIAA journal*, 6:1313–1319, 1968.

[11] A. Deraemaeker, I. Babuška, and P. Bouillard. Dispersion and pollution of the fem solution for the helmholtz equation in one, two and three dimensions. *Int. J. Numer. Methods Eng.*, 46:471–499, 1999.

[12] D. Fafalis and J. Fish. Computational aspects of dispersive computational continua for elastic heterogeneous media. *Comput. Mech.*, 56:931–946, 2015.

[13] V. Filonova, D. Fafalis, and J. Fish. Dispersive computational continua. *Comput. Methods Appl. Mech. Eng.*, 298:58–79, 2016.

[14] J. Fish and T. Belytschko. *A first course in finite elements*. John Wiley & Sons Ltd., Chichester, West Sussex, UK, 2007.

[15] J. Fish, W. Chen, and G. Nagai. Non-local dispersive model for wave propagation in heterogeneous media: one-dimensional case. *Int. J. Numer. Methods Eng.*, 54:331–346, 2002.

[16] J. Fish and S. Kuznetsov. Computational continua. *Int. J. Numer. Methods Eng.*, 84:774–802, 2010.

[17] B. Ganapathysubramanian and N. Zabaras. Modeling diffusion in random heterogeneous media: Data-driven models, stochastic collocation and the variational multiscale method. *J. Comput. Phys.*, 226:326–353, 2007.

[18] K. Garikipati and T. J. R. Hughes. A study of strain localization in a multiple scale framework-the one-dimensional problem. *Comput. Methods Appl. Mech. Eng.*, 159:193–222, 1998.

[19] K. Garikipati and T. J. R. Hughes. A variational multiscale approach to strain localization–formulation for multidimensional problems. *Comput. Methods Appl. Mech. Eng.*, 188:39–60, 2000.

[20] G. L. Goudreau and R. L. Taylor. Evaluation of numerical integration methods in elastodynamics. *Comput. Methods Appl. Mech. Eng.*, 2:69–97, 1973.

[21] S. K. Hong, B. I. Epureanu, and M. P. Castanier. Next-generation parametric reduced-order models. *Mech. Syst. Sig. Process.*, 37:403–421, 2013.

[22] T. Y. Hou and X. Wu. A multiscale finite element method for elliptic problems in composite materials and porous media. *J. Comput. Phys.*, 134:169–189, 1997.

[23] R. Hu and C. Oskay. Nonlocal homogenization model for wave dispersion and attenuation in elastic and viscoelastic periodic layered media. *J. Appl. Mech.*, 84:031003, 2017.

[24] R. Hu and C. Oskay. Spatial-temporal nonlocal homogenization model for transient anti-plane shear wave propagation in periodic viscoelastic composites. *Comput. Methods Appl. Mech. Eng.*, 342:1–31, 2018.

[25] R. Hu and C. Oskay. Multiscale nonlocal effective medium model for in-plane elastic wave dispersion and attenuation in periodic composites. *J. Mech. Phys. Solids*, 124:220–243, 2019.

[26] R. Hu, C. Prakash, V. Tomar, M. Harr, I. E. Gunduz, and C. Oskay. Experimentally-validated mesoscale modeling of the coupled mechanical–thermal response of ap-htpb energetic material under dynamic loading. *Int. J. Fract.*, 203:277–298, 2017.

[27] T. J. R. Hughes. *The finite element method: linear static and dynamic finite element analysis*. Dover Publications, Mineola, New York, 2000.

[28] T. J. R. Hughes, G. R. Feijóo, L. Mazzei, and J. B. Quincy. The variational multiscale method-a paradigm for computational mechanics. *Comput. Methods Appl. Mech. Eng.*, 166:3–24, 1998.

[29] T. Hui and C. Oskay. A high order homogenization model for transient dynamics of heterogeneous media including micro-inertia effects. *Comput. Methods Appl. Mech. Eng.*, 273:181–203, 2014.

[30] T. Hui and C. Oskay. Laplace-domain, high-order homogenization for transient dynamic response of viscoelastic composites. *Int. J. Numer. Methods Eng.*, 103:937–957, 2015.

[31] M. I. Hussein. Reduced bloch mode expansion for periodic media band structure calculations. *Proc. R. Soc. London, Ser. A*, 465:2825–2848, 2009.

[32] F. Ihlenburg and I. Babuška. Dispersion analysis and error estimation of galerkin finite element methods for the helmholtz equation. *Int. J. Numer. Methods Eng.*, 38:3745–3774, 1995.

[33] F. Ihlenburg and I. Babuška. Finite element solution of the helmholtz equation with high wave number part i: The h-version of the fem. *Comput. Math. Appl.*, 30:9–37, 1995.

[34] F. Ihlenburg and I. Babuska. Finite element solution of the helmholtz equation with high wave number part ii: the hp version of the fem. *SIAM J. Numer. Anal.*, 34:315–358, 1997.

[35] N. Kaina, F. Lemoult, M. Fink, and G. Lerosey. Negative refractive index and acoustic superlens from multiple scattering in single negative metamaterials. *Nature*, 525:77, 2015.

[36] A. Khelif, A. Choujaa, S. Benchabane, B. Djafari-Rouhani, and V. Laude. Guiding and bending of acoustic waves in highly confined phononic crystal waveguides. *Appl. Phys. Lett.*, 84:4400–4402, 2004.

[37] D. Krattiger and M. I. Hussein. Generalized bloch mode synthesis for accelerated calculation of elastic band structures. *J. Comput. Phys.*, 357:183–205, 2018.

[38] N. Lautersztajn-S and A. Samuelsson. On application of differential geometry to computational mechanics. *Comput. Methods Appl. Mech. Eng.*, 150:25–38, 1997.

[39] N. Lautersztajn-S and A. Samuelsson. Distortion measures and inverse mapping for isoparametric 8-node plane finite elements with curved boundaries. *Commun. Numer. Methods Eng.*, 14:87–101, 1998.

[40] J. Li, L. Fok, X. Yin, G. Bartal, and X. Zhang. Experimental demonstration of an acoustic magnifying hyperlens. *Nat. Mater.*, 8:931, 2009.

[41] C. Liu and C. Reina. Variational coarse-graining procedure for dynamic homogenization. *J. Mech. Phys. Solids*, 104:187 – 206, 2017.

[42] C. Liu and C. Reina. Dynamic homogenization of resonant elastic metamaterials with space/time modulation. *Comput. Mech.*, pages 1–15, 2018.

[43] Z. Liu, X. Zhang, Y. Mao, Y. Y. Zhu, Z. Yang, C. T. Chan, and P. Sheng. Locally resonant sonic materials. *Science*, 289:1734–1736, 2000.

[44] G. Ma and P. Sheng. Acoustic metamaterials: From local resonances to broad horizons. *Sci. Adv.*, 2:e1501595, 2016.

[45] M. Maldovan. Sound and heat revolutions in phononics. *Nature*, 503:209, 2013.

[46] A. Masud and R. A. Khurram. A multiscale/stabilized finite element method for the advection–diffusion equation. *Comput. Methods Appl. Mech. Eng.*, 193:1997–2018, 2004.

[47] A. Masud and K. Xia. A variational multiscale method for inelasticity: Application to superelasticity in shape memory alloys. *Comput. Methods Appl. Mech. Eng.*, 195:4512–4531, 2006.

[48] S. Meng and B. B. Guzina. On the dynamic homogenization of periodic media: Willis' approach versus two-scale paradigm. *Proc. R. Soc. A*, 474:20170638, 2018.

[49] G. W. Milton and J. R. Willis. On modifications of newton's second law and linear continuum elastodynamics. *Proc. R. Soc. London, Ser. A*, 463:855–880, 2007.

[50] S. H. Mousavi, A. B. Khanikaev, and Z. Wang. Topologically protected elastic waves in phononic metamaterials. *Nat. Commun.*, 6:8682, 2015.

[51] S. Nanthakumar, X. Zhuang, H. S. Park, C. Nguyen, Y. Chen, and T. Rabczuk. Inverse design of quantum spin hall-based phononic topological insulators. *J. Mech. Phys. Solids*, 125:550–571, 2019.

[52] H. Nassar, Q.-C. He, and N. Auffray. A generalized theory of elastodynamic homogenization for periodic media. *Int. J. Solids Struct.*, 84:139–146, 2016.

[53] S. Nemat-Nasser and A. Srivastava. Overall dynamic constitutive relations of layered elastic composites. *J. Mech. Phys. Solids*, 59:1953–1965, 2011.

[54] A. A. Oberai and P. M. Pinsky. A multiscale finite element method for the helmholtz equation. *Comput. Methods Appl. Mech. Eng.*, 154:281–297, 1998.

[55] C. Oskay. Variational multiscale enrichment for modeling coupled mechano-diffusion problems. *Int. J. Numer. Methods Eng.*, 89:686–705, 2012.

[56] C. Oskay. Variational multiscale enrichment method with mixed boundary conditions for modeling diffusion and deformation problems. *Comput. Methods Appl. Mech. Eng.*, 264:178–190, 2013.

[57] K. Pham, V. G. Kouznetsova, and M. G. D. Geers. Transient computational homogenization for heterogeneous materials under dynamic excitation. *J. Mech. Phys. Solids*, 61:2125–2146, 2013.

[58] H. T. Rathod and S. Kilari. General complete lagrange family for the cube in finite element interpolations. *Comput. Methods Appl. Mech. Eng.*, 181:295–344, 2000.

[59] H. T. Rathod and K. Sridevi. General complete lagrange interpolations with applications to three-dimensional finite element analysis. *Comput. Methods Appl. Mech. Eng.*, 190:3325–3368, 2001.

[60] D. Roca, O. Lloberas-Valls, J. Cante, and J. Oliver. A computational multiscale homogenization framework accounting for inertial effects: Application to acoustic metamaterials modelling. *Comput. Methods Appl. Mech. Eng.*, 330:415–446, 2018.

[61] D. Roca, D. Yago, J. Cante, O. Lloberas-Valls, and J. Oliver. Computational design of locally resonant acoustic metamaterials. *Comput. Methods Appl. Mech. Eng.*, 345:161–182, 2019.

[62] A. Sridhar, V. G. Kouznetsova, and M. G. D. Geers. Homogenization of locally resonant acoustic metamaterials towards an emergent enriched continuum. *Comput. Mech.*, 57:423–435, 2016.

[63] A. Sridhar, V. G. Kouznetsova, and M. G. D. Geers. A general multiscale framework for the emergent effective elastodynamics of metamaterials. *J. Mech. Phys. Solids*, 111:414–433, 2018.

[64] N. Stenger, M. Wilhelm, and M. Wegener. Experiments on elastic cloaking in thin plates. *Phys. Rev. Lett.*, 108:014301, 2012.

[65] L. L. Thompson and P. M. Pinsky. Complex wavenumber fourier analysis of the p-version finite element method. *Comput. Mech.*, 13:255–275, 1994.

[66] T. J. Truster and A. Masud. Primal interface formulation for coupling multiple pdes: a consistent derivation via the variational multiscale method. *Comput. Methods Appl. Mech. Eng.*, 268:194–224, 2014.

[67] J. R. Willis. Dynamics of composites. In *Continuum micromechanics*, pages 265–290. Springer, 1997.

[68] S. Yu, C. He, Z. Wang, F. Liu, X. Sun, Z. Li, H. Lu, M. Lu, X. Liu, and Y. Chen. Elastic pseudospin transport for integratable topological phononic circuits. *Nat. Commun.*, 9:3072, 2018.

[69] K. Y. Yuan, Y. S. Huang, H. T. Yang, and T. H. H. Pian. The inverse mapping and distortion measures for 8-node hexahedral isoparametric elements. *Comput. Mech.*, 14:189–199, 1994.

[70] S. Zhang and C. Oskay. Variational multiscale enrichment method with mixed boundary conditions for elasto-viscoplastic problems. *Comput. Mech.*, 55:771–787, 2015.

[71] S. Zhang and C. Oskay. Reduced order variational multiscale enrichment method for elasto-viscoplastic problems. *Comput. Methods Appl. Mech. Eng.*, 300:199–224, 2016.

[72] S. Zhang and C. Oskay. Reduced order variational multiscale enrichment method for thermo-mechanical problems. *Comput. Mech.*, 59:887–907, 2017.